

A Comparison of Hybrid Ensemble Transform Kalman Filter- 3DVAR and Ensemble Square-Root Filter Analysis Schemes

Xuguang Wang¹, Thomas M. Hamill², Jeffrey S. Whitaker², and Craig H. Bishop³

¹ *University of Colorado and NOAA-CIRES Climate Diagnostics Center, Boulder, CO*

² *NOAA-CIRES Climate Diagnostics Center, Boulder, CO*

³ *Naval Research Laboratory, Monterey, CA*

Submitted as an article to *Monthly Weather Review*

Sep. 10, 2005

Corresponding author address:

Dr. Xuguang Wang
NOAA-CIRES Climate Diagnostics Center
Boulder, CO 80305-3328
xuguang.wang@noaa.gov
phone: (303) 497-4434

Abstract

A hybrid ensemble transform Kalman filter (ETKF)-3DVAR analysis scheme is compared to an ensemble square-root filter (EnSRF) analysis scheme in a two-layer primitive equation model under perfect-model assumptions. The ETKF-3DVAR updates the ensemble mean with a hybridized ensemble covariance and the 3DVAR covariance, and it can be incorporated to the operational 3DVAR data assimilation framework conveniently. The ensemble perturbations are generated by the computationally efficient ETKF scheme. The EnSRF runs comparatively expensive parallel data assimilation cycles for each member and serially assimilates the observations. The EnSRF background-error covariance is estimated fully from the ensemble, and covariances are localized. The intent of this study is to determine whether the hybrid ETKF-3DVAR method provides much of the potential improved accuracy of the EnSRF.

It was found that depending on the norm, the analyses of the hybrid ETKF-3DVAR corresponding to the optimal linear combination coefficient were slightly less accurate or similar to the EnSRF using its optimal covariance localization scale. The ETKF-3DVAR system was less prone to spurious gravity wave activity than the EnSRF that requires covariance localization. Maximal growth in the ETKF ensemble perturbation space exceeded that in the EnSRF ensemble perturbation space. The skill of the ETKF ensemble variance to estimate the ensemble mean error variance is similar to that of the EnSRF ensemble. It was also found that applying covariance localization to the ensemble part of the hybrid error covariance when updating the mean did not improve its analysis. The hybrid ETKF-3DVAR approach is thus judged to be a promising, less expensive approach to utilize ensemble forecasts effectively in data assimilations.

1. Introduction

Variational techniques are now almost universally used for operational atmospheric data assimilation in either its three-dimensional form (3DVAR; e.g., Parrish and Derber 1992; Courtier et al. 1998; Gauthier et al. 1998; Cohn et al. 1998) or its four-dimensional form (4DVAR, e.g., Courtier et al. 1994; Rabier et al. 1998, 2000). Both 3DVAR and 4DVAR assimilations generally begin in each update cycle with nearly homogeneous, isotropic, and stationary background error covariance model¹, which only provides a crude estimate of the actual flow-dependent forecast error structure. Currently, 3DVAR is still utilized in many operational centers due to its computational efficiency and algorithmic simplicity.

Recently, a variety of techniques have been explored to relax the restrictions on the background-error covariance model in data assimilations. For 3DVAR, techniques are being developed that make it possible to include some spatial inhomogeneity, non-stationarity, and anisotropy (e.g., Riishøjgaard 1998, Wu et al. 2002, Purser et al. 2003, Liu et al. 2005). A different approach is to use ensemble-based data assimilation techniques, where the background-error covariances are estimated from an ensemble of short-term forecasts (e.g., Evensen 1994, Burgers et al. 1998, Houtekamer and Mitchell 1998, 2001, 2005, Hamill and Snyder 2000, Anderson 2001, Whitaker and Hamill 2002, Ott et al. 2003, Tippett et al. 2003, Snyder and Zhang 2003, Hamill and Whitaker 2005, Tong and Xue 2005). For reviews on ensemble-based techniques, see Evensen (2003), Lorenc (2003), and Hamill (2005).

¹ Hereafter, we use the term “3DVAR covariance” to indicate time-invariant, isotropic and homogeneous background covariance, as those assumptions are commonly used in the 3DVAR scheme.

The presumed benefit of utilizing these ensemble-based techniques is their ability to provide a flow-dependent estimate of the forecast-error covariance so that the relative contribution of the guess and the observations are more appropriately weighted. Another potential benefit is that the processes of ensemble forecasting and data assimilation are unified. In many controlled tests with simple models and simulated observations, ensemble-based methods have demonstrated dramatically improved analysis skill. However, tests of ensemble-based methods in a realistic operational environment are still at a preliminary stage. Recent global, real-data experiments show that the ensemble Kalman filter (EnKF; Houtekamer et al. 2005, Houtekamer and Mitchell 2005) and the ensemble-square root filter (EnSRF; Whitaker and Hamill 2005), provide comparable or slightly better results to operational 3DVAR algorithms.

Many of the current ensemble-based data assimilation techniques serially process the observations, so the computational expense of the algorithm scales linearly with the number of observations, unlike in 3DVAR and 4DVAR. This may make these methods unattractive for use in operational numerical weather prediction centers, where the numbers of available observations are increasing rapidly each year.

Is there a method that can take advantage of the computational efficiency of the 3DVAR and also benefits from the ensemble-estimated error covariance? Recently, Hamill and Snyder (2000) proposed a hybrid EnKF-3DVAR method (hereafter HS). In this scheme, the background-error covariance was obtained by explicitly weighting a flow-dependent background-error covariance from the ensemble together with the standard error-covariance estimate from 3DVAR. Each ensemble member is then updated variationally with perturbed observations. Subsequently, Lorenc (2003) and

Buehner (2005) discussed how an ensemble-based covariance model could be adapted conveniently to the variational framework by extending the control variables. A proof of the equivalence of the hybrid method realized by the augmented control variables and by directly weighting the covariances was recently provided in Wang et al. (2005).

More recently, Etherton and Bishop (2004) tested a hybrid ensemble transform Kalman filter (ETKF)-3DVAR assimilation scheme, which is a variation of the HS scheme. Unlike the HS scheme where K parallel data assimilation cycles for the K members were required, in the hybrid ETKF-3DVAR, a single update of the mean was performed, and the ETKF transformed the background perturbations into analysis perturbations in a computationally efficient manner. The ETKF, was proposed by Bishop et al. (2001). It has been demonstrated to be a useful tool for targeted observations (Majumdar et al. 2001, 2002ab). Wang and Bishop (2003) and Wang et al. (2004) also have shown that the ETKF provides an inexpensive yet demonstrably superior scheme to the breeding method (Toth and Kalnay 1993, 1997) for generating perturbed initial conditions for ensemble forecasts. Etherton and Bishop (2004) found that the performance of the hybrid scheme using the ETKF ensemble was comparable to that obtained using considerably more expensive ensemble generation schemes.

The purpose of this study is to further explore the potential skill of the hybrid ETKF-3DVAR analysis scheme by comparing it with the EnSRF, one of the more well-tested ensemble-based assimilation schemes (Whitaker and Hamill 2002; Whitaker and Hamill 2005; Snyder and Zhang 2003; Zhang et al. 2004; Ott et al. 2004; Szunyogh et al. 2005; Houtekamer and Mitchell 1998, 2001, 2005; Houtekamer et al. 2005). If the ETKF-3DVAR can realize much of the improvement by the EnSRF relative to the

3DVAR, then it may be more appealing to the operational centers as it is convenient to be adapted in the current variational framework, computationally less expensive, and relatively low risk – it can perform no worse than 3DVAR, for its blend of covariances can always be adjusted to exclude the contribution of the ensemble.

As an initial attempt to investigate the potential skill of the hybrid ETKF-3DVAR relative to the EnSRF, we first conduct our experiments here with a two-layer primitive equation model under the perfect-model assumption. Such a test design will isolate whether the hybrid ETKF-3DVAR with no covariance localization required will generate analyses similar in skill to the EnSRF, which requires covariance localization to prevent filter divergence (Houtekamer and Mitchell 2001, Hamill et al. 2001). Future work by the co-authors will extend this research to compare the methods in simulations including model error.

The rest of the article is organized as follows. In section 2, we briefly review the hybrid ETKF-3DVAR and the EnSRF analysis schemes. Section 3 describes the experimental design. Results of comparing the two schemes are reported in section 4. Section 5 concludes the paper.

2. The hybrid ETKF-3DVAR and the EnSRF analysis schemes

a. The hybrid ETKF-3DVAR scheme

Figure 1 illustrates how the hybrid ETKF-3DVAR data assimilation cycle works. Start with an ensemble of K background forecasts at time t_0 . The following four steps are then repeated for each data assimilation cycle. 1) Update the ensemble mean or a high resolution control forecast by the hybrid ETKF-3DVAR background-error covariance. 2)

Update the forecast perturbations using the ETKF transformation matrix. 3) Add the updated ensemble perturbations to the updated ensemble mean to generate K initial ensemble members. 4) Make K forecasts starting from the K initial ensemble members forward to the next analysis time.

When updating the mean, the background error covariance \mathbf{P}^b is approximated by a linear combination of the sample covariance matrix of the ETKF forecast ensemble \mathbf{P}^e and the 3DVAR covariance matrix \mathbf{B} , i.e.,

$$\mathbf{P}^b = (1 - \alpha)\mathbf{P}^e + \alpha\mathbf{B}, \quad (1)$$

where α is the weighting coefficient, $0 \leq \alpha \leq 1$, and \mathbf{P}^e is given by

$$\mathbf{P}^e = \frac{\mathbf{X}^b (\mathbf{X}^b)^T}{K - 1}, \quad (2)$$

where the columns of \mathbf{X}^b contain K ensemble perturbations from the mean, \mathbf{x}_i^b , $i = 1, \dots, K$.

As mentioned in the previous section and section 5, previous work (Lorenz 2003; Buehner 2005; Barker 1999; Wang et al. 2005) has shown that hybridizing the ensemble covariance in the existing operational 3DVAR framework with preconditioning can be achieved conveniently. Since development of this variational code for the two-layer primitive equation model is time consuming and the intent of this study is to demonstrate the effect of the hybrid covariance model, we employ the Kalman-filter state update equation instead, which can also be derived from the 3DVAR cost function (Daley 1991). It will provide an identical solution under the assumption of normality of error distributions and linear observation operator. In an ensemble construct, this equation

updates the ensemble-mean forecast $\bar{\mathbf{x}}^b$ to the new observations \mathbf{y} to obtain the ensemble-mean analysis $\bar{\mathbf{x}}^a$, i.e.,

$$\bar{\mathbf{x}}^a = \bar{\mathbf{x}}^b + \mathbf{P}^b \mathbf{H}^T (\mathbf{H} \mathbf{P}^b \mathbf{H}^T + \mathbf{R})^{-1} (\mathbf{y} - \mathbf{H} \bar{\mathbf{x}}^b), \quad (3)$$

where \mathbf{H} is the observation operator mapping from the model state variables to the observed variables, here presumed linear, \mathbf{R} is the observation-error covariance matrix, and \mathbf{P}^b is given by equation (1). Note as in EnKF framework (Evensen 1994; Houtekamer and Mitchell 1998), there is no need to compute and store the full matrix \mathbf{P}^b . Instead we first form $\mathbf{B} \mathbf{H}^T$ and $\mathbf{H} \mathbf{B} \mathbf{H}^T$ (see section 3b for details), and calculate $\mathbf{P}^e \mathbf{H}^T$ and $\mathbf{H} \mathbf{P}^e \mathbf{H}^T$ from the ensemble. Then we use the linear coefficient α as in (1) to form $\mathbf{P}^b \mathbf{H}^T$ and $\mathbf{H} \mathbf{P}^b \mathbf{H}^T$, i.e.,

$$\mathbf{H} \mathbf{P}^b \mathbf{H}^T = (1 - \alpha) \mathbf{H} \mathbf{P}^e \mathbf{H}^T + \alpha \mathbf{H} \mathbf{B} \mathbf{H}^T, \quad (4)$$

$$\mathbf{P}^b \mathbf{H}^T = (1 - \alpha) \mathbf{P}^e \mathbf{H}^T + \alpha \mathbf{B} \mathbf{H}^T. \quad (5)$$

With $\alpha=1$, equ. (3) provides an ensemble-mean 3DVAR analysis. Note as in Etherton and Bishop (2004), before applying the hybrid formulations (4) and (5), steps are taken to ensure that the traces of \mathbf{P}^e and \mathbf{B} are equivalent in the observation space. For a detailed explanation of this, see section 3b.

In the hybrid analysis scheme, the ensemble perturbations are updated by the ETKF. The ETKF transforms the matrix of forecast perturbations \mathbf{X}^b into a matrix of analysis perturbations \mathbf{X}^a , whose columns contain K analysis perturbations, \mathbf{x}_k^a , $k = 1, K$. The transformation happens through the post-multiplication by the matrix \mathbf{T} , that is,

$$\mathbf{X}^a = \mathbf{X}^b \mathbf{T}. \quad (6)$$

The transformation matrix is chosen to ensure that the analysis-error covariance formed from the outer product of the transformed perturbations will be precisely equal to the true analysis-error covariance, assuming that eq. (2) denotes the true forecast-error covariance, all errors are normally distributed, and \mathbf{H} is linear. As shown in Bishop et al. (2001), Wang and Bishop (2003) and Wang et al. (2004), a precise spherical simplex solution of \mathbf{T} is

$$\mathbf{T} = \mathbf{C}(\mathbf{\Gamma} + \mathbf{I})^{-1/2} \mathbf{C}^T, \quad (7)$$

where \mathbf{C} contains the eigenvectors and $\mathbf{\Gamma}$ the eigenvalues of the $K \times K$ matrix $(\mathbf{x}^b)^T \mathbf{H}^T \mathbf{R}^{-1} \mathbf{H} \mathbf{x}^b$ and \mathbf{I} is the identity matrix. For the ensemble size K of 100 or less, the computation of (7) is relatively inexpensive.

When K is significantly smaller than the rank γ of the true forecast-error covariance, (2) is a poor approximation of the background-error covariances. The analysis-error covariance estimated through the ETKF-transformed perturbations is thus far from optimal. In the first implementation of the ETKF, the ensemble of analyzed deviations \mathbf{x}^a were dramatically inflated to compensate for the small ETKF-estimated analysis-error variance (Wang and Bishop 2003). As discussed in Appendix A, this bias can be significantly ameliorated by accounting for (a) the fact that the sample covariance of K forecast trials systematically overestimates the true error variance within the ensemble subspace when $K \ll \gamma$, and (b) the expected angle subtended between ensemble-based eigenvectors and true eigenvectors. Based on these arguments, the ETKF transformation matrix \mathbf{T} is updated to

$$\mathbf{T} = \mathbf{C}(\rho \mathbf{\Gamma} + \mathbf{I})^{-1/2} \mathbf{C}^T, \quad (8)$$

where the scalar factor ρ is the fraction of the forecast error variance projected onto the ensemble subspace. It is estimated by

$$\rho = \frac{\overline{\left(\mathbf{R}^{-1/2} \mathbf{y} - \tilde{\mathbf{H}} \bar{\mathbf{x}}^b\right)^T \mathbf{E} \mathbf{E}^T \left(\mathbf{R}^{-1/2} \mathbf{y} - \tilde{\mathbf{H}} \bar{\mathbf{x}}^b\right)} - (K-1)}{\overline{\left(\mathbf{R}^{-1/2} \mathbf{y} - \tilde{\mathbf{H}} \bar{\mathbf{x}}^b\right)^T \left(\mathbf{R}^{-1/2} \mathbf{y} - \tilde{\mathbf{H}} \bar{\mathbf{x}}^b\right)} - p}, \quad (9)$$

where p is the number of observations, $\tilde{\mathbf{H}}$ is the normalized observation operator

$\tilde{\mathbf{H}} = \mathbf{R}^{-1/2} \mathbf{H}$, and the columns of \mathbf{E} contain the eigenvectors of the ensemble covariance in normalized observation space. As shown in eq. (12) of Bishop et al. (2001),

$$\mathbf{E} = \tilde{\mathbf{H}} \mathbf{X}^b \mathbf{C} \mathbf{\Gamma}^{-1/2} / \sqrt{K-1}. \quad (10)$$

The over bar in (9) represents the average over some independent samples. In this experiment it is the average over two weeks' computations prior to each assimilation time. For derivations of (8) and (9), please refer to appendices A and B respectively. A more detailed discussion about the bias-ameliorated ETKF formulation will be given in a forthcoming paper. Note no covariance localization is applied in this ETKF, unlike most other ensemble data assimilation methods.

The maximal likelihood inflation method (for details see Wang and Bishop 2003) is applied. The idea is to multiply the initial perturbations obtained at time t_i by an online estimated inflation factor Π_i , i.e.,

$$\mathbf{X}_i^a = \mathbf{X}_i^f \mathbf{T}_i \Pi_i, \quad (11)$$

to ensure that at time t_{i+1} the background ensemble forecast variance is consistent with the ensemble-mean background-error variance over global observation sites. Specifically, define $\tilde{\mathbf{d}}_i$ as the innovation vector at t_i , normalized by the square root of the observation

error covariance matrix, that is, $\tilde{\mathbf{d}}_i = \mathbf{R}^{-1/2}(\mathbf{y}_i - \mathbf{H}\bar{\mathbf{x}}_i^b)$, where \mathbf{y}_i is the observation vector at t_i and $\mathbf{H}\bar{\mathbf{x}}_i^b$ is the ensemble mean background forecast valid at the time t_i mapped into observation space by the observation operator \mathbf{H} . Given that the inflation factor at t_{i-1} was Π_{i-1} , the inflation factor for the transformed perturbation at t_i is obtained by first checking if $\tilde{\mathbf{d}}_i^T \tilde{\mathbf{d}}_i$ is equal to $Tr(\tilde{\mathbf{H}}\mathbf{P}_i^e \tilde{\mathbf{H}}^T + \mathbf{I})$, where Tr denotes the trace. If not, we need to introduce a parameter c_i so that

$$\tilde{\mathbf{d}}_i^T \tilde{\mathbf{d}}_i = Tr(\tilde{\mathbf{H}}c_i \mathbf{P}_i^e \tilde{\mathbf{H}}^T + \mathbf{I}). \quad (12)$$

Then the inflation factor Π_i is defined as

$$\Pi_i = \Pi_{i-1} \sqrt{c_i}. \quad (13)$$

This rescaling of the initial perturbations by (13) attempts to correct the spread of the set of forecast ensemble perturbations at time t_{i+1} by using the rescaling factor that would have produced a proper forecast ensemble spread at t_i if it had been applied to the transformed perturbations at t_{i-1} . From (12)

$$c_i = \frac{\tilde{\mathbf{d}}_i^T \tilde{\mathbf{d}}_i - p}{Tr(\tilde{\mathbf{H}}\mathbf{P}_i^e \tilde{\mathbf{H}}^T)}, \quad (14)$$

where p is the number of observations. From equation (13), Π_i is a product of these c parameters from the first forecast at time t_1 to that at time t_i , that is,

$$\Pi_i = \sqrt{c_1 c_2 \cdots c_i}. \quad (15)$$

Implicitly in (12), we assume $\tilde{\mathbf{d}}_i^T \tilde{\mathbf{d}}_i = Tr < \tilde{\mathbf{d}}_i \tilde{\mathbf{d}}_i^T >$, which requires the number of independent elements in the innovation vector $\tilde{\mathbf{d}}_i$ to be large. Real-time global

observational network meets this assumption well (Dee 1995). Since the number of observations in our experiment is rather limited, we replace $\tilde{\mathbf{d}}_i^T \tilde{\mathbf{d}}_i$ in (12) and (14) by using the average of squared innovation vectors two weeks prior to time t_i , denoted as $\overline{\tilde{\mathbf{d}}^T \tilde{\mathbf{d}}}_{prior_{t_i}}$ (see discussion in Appendix B also). Thus (14) becomes

$$c_i = \frac{\overline{\tilde{\mathbf{d}}^T \tilde{\mathbf{d}}}_{prior_{t_i}} - p}{Tr(\tilde{\mathbf{H}} \mathbf{P}_i^e \tilde{\mathbf{H}}^T)}. \quad (16)$$

In the following hybrid data assimilation experiments, c_i fluctuates about unity with the averaged rms deviation about 0.2.

b. The EnSRF analysis scheme

The EnSRF was fully described in Whitaker and Hamill (2002). It is one of the simpler implementations of a class of ensemble square-root filters which includes the ETKF (Tippett 2003). Whereas the primary advantage of the hybrid ETKF-3DVAR is its low computational expense, the comparative advantage of the EnSRF is its relative algorithmic simplicity and the consistency of the prior background error covariances used to update the mean and the ensemble. In the EnSRF, covariance localization is necessary to avoid filter divergence (Houtekamer and Mitchell 2001; Hamill et al. 2001) and to improve the analysis accuracy. However, covariance localization can produce imbalanced initial conditions (e.g., Mitchell et al. 2002; Lorenc 2003). For the hybrid ETKF-3DVAR, no covariance localization is required on the ETKF as hybridizing the 3DVAR covariance adds in extra degrees of freedom and thus stabilizes the filter. Note

covariance localization can be applied for the ETKF when updating the mean (Section 4a).

The EnSRF serially assimilates observations for each member, and the ensemble of perturbations updated by the previous observations are used to model the background-error covariance for assimilating the next observation. The EnSRF update equations are as follows:

$$\bar{\mathbf{x}}^a = \bar{\mathbf{x}}^b + \mathbf{K}(\mathbf{y} - \mathbf{H}\bar{\mathbf{x}}^b), \quad (17)$$

$$\mathbf{x}_i'^a = (\mathbf{I} - \tilde{\mathbf{K}}\mathbf{H})\mathbf{x}_i'^b. \quad (18)$$

Here \mathbf{K} is the Kalman gain modified by the covariance localization,

$$\mathbf{K} = (\boldsymbol{\rho}_s \circ \mathbf{P}^e \mathbf{H}^T) (\boldsymbol{\rho}_s \circ \mathbf{H} \mathbf{P}^e \mathbf{H}^T + \mathbf{R})^{-1}, \quad (19)$$

where the operation $\boldsymbol{\rho}_s \circ$ denotes a Schur product of a correlation matrix $\boldsymbol{\rho}_s$ with the covariance model generate by the ensemble. For horizontal localization, one such correlation matrix can be constructed using Gaspari and Cohn's (1999) approximately Gaussian-shaped function with local support, which will be used here. When sequentially processing independent observations, \mathbf{K} , $\tilde{\mathbf{K}}$, and $\mathbf{P}^e \mathbf{H}^T$ are all vectors with the same number of elements as the model state vector, and $\mathbf{H} \mathbf{P}^e \mathbf{H}^T$ and \mathbf{R} are scalars. The reduced gain becomes

$$\tilde{\mathbf{K}} = \left(1 + \sqrt{\frac{\mathbf{R}}{\mathbf{H} \mathbf{P}^e \mathbf{H}^T + \mathbf{R}}} \right)^{-1} \mathbf{K}. \quad (20)$$

A global inflation factor was computed and applied to the initial EnSRF ensemble using the same method as that used for the ETKF ensemble.

3. Experiment design

a. Model, observations, and ensemble configuration

In this study, we ran a dry, global, two-layer primitive equation model (Zou et al. 1993). It was previously used in Hamill et al. (2001) and Hamill and Whitaker (2005) for ensemble data assimilation experiments in both a perfect-model and imperfect model contexts. The model is spectral and the model state vector includes spectral coefficients of vorticity and divergence at two levels, and two layer thicknesses $\Delta\pi_1$ and $\Delta\pi_2$, where π is the Exner function. There is a simple, zonal wavenumber 2 terrain. The model is forced by Newtonian relaxation to a prescribed interface Exner function. A fourth order Runge-Kutta scheme is used for numerical integration, and ∇^8 hyperdiffusion is used. The parameters chosen are the same as in Hamill and Whitaker (2005). The model was run at T31 resolution, which produces a relatively slow error-doubling time of about 4 days. The perfect-model assumption was made in the following experiment. For detailed model dynamics characteristics, please refer to Hamill and Whitaker (2005).

Observations of interface π and surface π were taken at a set of nearly equally spaced locations on a spherical geodesic grid (Fig. 2). The 362 observations of each consisted of the T31 true state plus errors drawn from a distribution with zero mean and standard deviation of $8.75 \text{ Jkg}^{-1} \text{ K}^{-1}$ for interface π and $0.875 \text{ Jkg}^{-1} \text{ K}^{-1}$ for surface π , respectively. The numbers chosen were about one quarter of the globally averaged climatological spread of the nature runs. Observation errors were constructed to be independent spatially and temporally, and observations were assimilated every 24h.

In all the experiments, the ensemble size was 50 members. The ensemble was initialized with random draws from the model climatology. The data assimilation was conducted for 150-day period, and the statistics were accumulated over the last 100 days.

b. 3DVAR error covariance

In this experiment, we used a technique for developing a static 3DVAR error covariance model similar to ones described in Evensen (2003), Zhang and Anderson (2003) and Hamill and Whitaker (2005). In this experiment, the 3DVAR background-error covariance was formed from a large inventory of historical forecast errors; in other words, actual background forecast errors were collected over many separate times. To obtain a realistic 3DVAR error- covariance model in this framework, the following steps were iterated until the analysis-error statistics were stable: 1) collect the background error samples from the data assimilation cycle. For the first iteration, the samples were obtained from the 24h ensemble mean forecast errors of the lowest-error EnSRF experiment; 2) build a range of possible 3DVAR covariance models $\mathbf{H}\mathbf{B}^s\mathbf{H}^T$ and $\mathbf{B}^s\mathbf{H}^T$ from the sample covariances of these samples and applying a range of different potential covariance localization scales to reduce the sampling error; 3) run a 3DVAR data assimilation cycle for each of these background-error covariance models with an online estimated rescaling factor specified below; 4) choose the 3DVAR cycle with the smallest root-mean square (rms) analysis error; and 5) return to step 1.

Note in step 3, as in Etherton and Bishop (2004), during each assimilation cycle we rescale the 3DVAR covariance models so that in the normalized observation space, the total variance of the 3DVAR covariance model is consistent with the total forecast

error variance. To be specific, at data assimilation time t_i , we seek a rescaling factor f_i that satisfies

$$\overline{\tilde{\mathbf{d}}^T \tilde{\mathbf{d}}}_{prior_i} = \text{trace}(\tilde{\mathbf{H}} f_i \mathbf{B}^s \tilde{\mathbf{H}}^T + \mathbf{I}), \quad (21)$$

where $\overline{\tilde{\mathbf{d}}^T \tilde{\mathbf{d}}}_{prior_i}$ is defined the same as in (16). The subsequent rescaled 3DVAR error covariances at t_i are $\mathbf{H} \mathbf{B}_i \mathbf{H}^T = \mathbf{H} f_i \mathbf{B}^s \mathbf{H}^T$ and $\mathbf{B}_i \mathbf{H}^T = f_i \mathbf{B}^s \mathbf{H}^T$. Note the rescaling strategies adopted make traces of the ensemble covariance and the 3DVAR error covariance are approximately equal. Thus, the coefficient α in (1), (4) and (5) gives a clearer indication of the relative weights assigned on the error correlations given by the ensemble and the 3DVAR.

Following the above steps, the rms analysis error of the 3DVAR run converged after the second iteration with 250 error samples and a Gaspari and Cohn (1999) horizontal localization which tapered to zero at 15000 km. This error covariance model together with the rescaling strategy was adopted as the 3DVAR background error covariance in the subsequent hybrid experiments. The 3DVAR error covariance built this way is an approximation to the operational 3DVAR. For example, since in operations the truth is unknown, the samples are collected from series of 24h minus 12h forecasts or analysis (Parish and Derber 1992). Constraints are imposed in the operational 3DVAR to maintain balance. The use of localization to build the 3DVAR covariance in this experiment may degrade the balance implicit in short term forecast errors.

4. Results

a. Analysis errors

In this section, we evaluate the characteristics of the analysis errors for the hybrid ETKF-3DVAR and the EnSRF analysis schemes. Fig. 3 shows the rms analysis error in the norm of kinetic energy, upper-layer thickness $\Delta\pi_2$, and the surface pressure π . Definitions of these norms are provided in Hamill and Whitaker (2005). The black bars correspond to the results of the hybrid ETKF-3DVAR as a function of the weighting coefficient, α . The grey bars correspond to the rms analysis errors of the EnSRF with respect to different covariance localization length scale. The white bar is the result for the 3DVAR. Note the difference between the 3DVAR and the $\alpha = 1.0$ experiments is that the background forecast for the former is from the single control forecast whereas for the latter it is from the ETKF ensemble mean forecast.

The optimal linear combination coefficient α for the hybrid ETKF-3DVAR was 0.4 for all three norms. When the background error covariance was purely from the 3DVAR, i.e., $\alpha = 1.0$, the analysis error was less than the error of the 3DVAR control simulation, which presumably was because the background forecast from the ensemble mean was more accurate than the control run; a similar result was shown in the perturbed-observation experiments in Hamill et al. (2000). The localization scale that produced the smallest rms error for the EnSRF in this experiment was ~ 15000 km – 25000 km. In all three measures, the best performance of the hybrid ETKF-3DVAR was slightly worse than that of the EnSRF. However, approximately 90% of the improvement of the EnSRF over the 3DVAR was achieved by the hybrid ETKF-3DVAR. As expected, the hybrid with the coefficient of 0.0 and the EnSRF with no localization both exhibited filter divergence due to the sampling error of the limited ensemble size. Although the old ETKF using (7) with $\alpha = 0.0$ diverged with similar rapidity to the EnSRF with no

localization, the new ETKF using (8) with $\alpha = 0.0$ diverged much more slowly (not shown). This indicated that with a limited ensemble size, the new ETKF sampled the analysis error better than both the un-localized EnSRF and the old ETKF.

The optimal localization scale for the EnSRF was larger than what may have been expected by other studies (e.g., Hamill et al. 2001; Houtekamer et al. 2005). The possible reasons are a) the model resolution in this experiment was coarse, T31, and the covariance localization scale for a coarse-resolution model may be larger than that for a fine-resolution model that can resolve small-scale features; b) the optimal localization scale for the EnSRF is longer than that for the EnKF, since the EnKF introduces much noise through the perturbation of observations (Whitaker and Hamill 2002); and c) the two-layer primitive equation model in this experiment did not include an initialization step, to efficiently damp the gravity-wave noise generated by the imbalance due to a short localization scale, and the explicit 4th-order Runge Kutta time integration scheme also failed to damp these fast-propagating wave motions. Thus an imbalanced background inherited from the previous assimilation cycle together with the imbalance introduced by the EnSRF assimilation may have accumulated during the assimilation cycles, more acutely so with a more severe localization. Perhaps this aspect could have been better controlled with a different time integration scheme or an explicit initialization.

In the above results of the hybrid ETKF-3DVAR, no covariance localization was applied for the ensemble covariance when updating both the mean and the perturbations. Although covariance localization is not required by the hybrid ETKF-3DVAR, one can choose to apply it onto the ensemble covariance when updating the mean to see whether it will improve the hybrid analysis accuracy further. Our results (not shown) indicated

that none of the hybrid ETKF-3DVAR experiments with covariance localization applied produced better analyses than the hybrid experiment with $\alpha = 0.4$ and no localization, although appropriately chosen covariance localization had positive impact for small α . For example, at $\alpha = 0.0$, filter divergence was avoided when covariance localization was used. At small α , e.g., $\alpha = 0.2$, applying covariance localization with scale of 25000km reduced the analysis error by 6% for the surface π and kinetic energy norms, and by 11% for the $\Delta\pi_2$ norm, whereas applying relatively smaller localization scales such as 15000km degraded the analysis skill by 22%, 40% and 2% for the surface π , kinetic energy and $\Delta\pi_2$ norms respectively. Applying 5000km localization scale degraded the analysis skill even more. At relatively larger α , e.g., $\alpha = 0.4$, applying the covariance localization performed the same or worse than with no localization. As covariance localization can potentially generate imbalanced initial conditions, in the following we only show experiment results of the hybrid ETKF-3DVAR with no covariance localization.

b. Similarity of hybrid and EnSRF covariance models

To demonstrate that with the ensemble covariance incorporated in the hybrid ETKF-3DVAR the background error covariance is flow-dependent, we performed single-observation experiments and plotted the analysis increment associated after assimilating a single prespecified observation. For illustration, we conducted the experiment based on the background ensemble at the 100th data assimilation cycle from each experiment above. Fig. 4 and Fig. 5 show the results for the hybrid ETKF-3DVAR with the optimal coefficient $\alpha = 0.4$ and the EnSRF with the optimal covariance localization scale of 25000 km. The contours are the background ensemble mean of upper layer zonal wind,

meridional wind and thickness, at the 100th cycle. The colors are the analysis increment from the assimilation of one $\Delta\pi_2$ observation with the value of $3 \text{ Jkg}^{-1} \text{ K}^{-1}$ smaller than the mean background at 47° N, 108° W. Both increments from the hybrid and the EnSRF were aligned along the flow pattern, and the wind increment appeared to be dynamically consistent with the interface height increment, e.g., a cyclonic wind was associated with a decrease of layer thickness around the observation site. As expected, the corresponding increment for the hybrid with background-error covariance purely estimated by the 3DVAR ($\alpha=1.0$) was relatively confined and did not correspond to the orientation of the flow pattern (not shown), which is consistent with previous studies (e.g., Hamill and Snyder 2000).

c. Comparison of maximal perturbation growth rates

A desirable property of an ensemble of initial conditions is an appropriately rapid growth of subsequent forecast perturbation. We measured the error-growth characteristics of various ensembles by calculating the fastest growth within the ensemble subspace during the first 24 h. First we assumed for a short-term forecast that the dynamic operator \mathbf{M} was linear, that is,

$$\mathbf{X}^b = \mathbf{M} \mathbf{X}^a. \quad (22)$$

We then identified the direction in the initial ensemble perturbation subspace where the subsequent amplification was maximized in a chosen norm, that is, we found the vector of linear combination coefficients \mathbf{b} to apply to the initial perturbation such that

$$\max \frac{\mathbf{b}^T (\mathbf{X}^b)^T \mathbf{S} \mathbf{X}^b \mathbf{b}}{\mathbf{b}^T (\mathbf{X}^a)^T \mathbf{S} \mathbf{X}^a \mathbf{b}}. \quad (23)$$

Here \mathbf{S} defines a particular norm. In this case we choose a global kinetic-energy norm and \mathbf{S} is a diagonal matrix. As shown in Bishop and Toth (1999), \mathbf{b} actually was the leading eigenvector of $\boldsymbol{\beta}^{-1/2} \mathbf{D}^T (\mathbf{X}^b)^T \mathbf{S} \mathbf{X}^b \mathbf{D} \boldsymbol{\beta}^{-1/2}$ where $\boldsymbol{\beta}$ and \mathbf{D} were the eigenvalue and eigenvector matrices of $(\mathbf{X}^a)^T \mathbf{S} \mathbf{X}^a$, and the corresponding eigenvalue was the maximal growth.

Fig. 6 shows the 24-h maximal growth in the global kinetic-energy norm within the ETKF and EnSRF ensemble subspaces. For the ETKF, the maximal growth corresponding to the optimal performance in rms analysis error measure ($\alpha = 0.4$) was larger than that of the optimal EnSRF (15000 km \sim 25000 km localization scale). While the maximal growth for the ETKF with different linear combination coefficients were similar, the maximal growth of the EnSRF varied with the localization scale applied. In general, the maximal growth decreased with more severe localization.

d. Initial-condition balance.

The EnSRF's slower growth under more severe localization in Fig. 6 may have been due to the imbalanced perturbations induced by the covariance localization (Mitchell et al. 2002, Lorenc 2003, Houtekamer and Mitchell 2005). In an operational data assimilation system, an explicit or implicit initialization is typically utilized, otherwise imbalances between the mass, momentum, and diabatic heating in the analysis can produce large-amplitude gravity waves. However, initialization requires extra computational cost and also it may degrade the analysis. Hence a data assimilation technique that itself can produce balanced initial condition is desirable.

The mean absolute tendency of surface pressure (Lynch and Huang 1992) is a useful diagnostic of the amount of balance/imbalance for an analysis generated by a data assimilation scheme. Surface π is the quantity analogous to the surface pressure in the two-layer primitive equation model. To examine surface π tendencies, we re-ran forecasts from the analysis ensembles to 24-h lead, producing output every hour. We then calculated the hourly surface Exner function tendencies. Fig. 7 shows the mean absolute tendency of the hourly surface π averaged over global grids, all ensemble members, all times, and the 23 hourly tendency snapshots from the forecast. As expected, the EnSRF tendencies were larger than the true tendency, and this discrepancy was greater when the localization length scale was shorter. For the hybrid, the initial analyses were much more balanced when weighting the unlocalized ETKF covariances than when weighting the localized 3DVAR covariances [an operational 3DVAR with a more carefully designed background-error covariance model may be more balanced than our simplified 3DVAR covariance model implemented here]. The optimal hybrid ($\alpha = 0.4$) was more balanced than the EnSRF with optimal localization (15000 - 25000 km). This result suggests that relative to the hybrid ETKF-3DVAR, the EnSRF may be more in need of an explicit initialization step or to use a time integration scheme with extra numerical damping of gravity waves.

e. Spread-skill relationships.

To measure a spread-skill relationship, we used a method similar to that used in Wang and Bishop (2003). We first produced a scatterplot whose ordinate and abscissa are

the squared analysis error and the analysis ensemble variance for a particular variable of interest, respectively. We collected such points over all grid points and for all time samples. We then divided these points into four equally populated bins, arranged in order of increasing ensemble variance. Next, we averaged the squared analysis error and analysis ensemble variance for each bin and took its square root. Connecting the points then yields a curve describing the relationship between the analysis ensemble spread and the rms analysis error. Fig. 8 shows an example of such curves of surface π for the hybrid with $\alpha = 0.4$ and the EnSRF with localization length scale equal to 15000 km. There are two aspects of the curve that we are interested to examine. First, after further averaging the values of the four points, we found that both schemes' ensemble spread were approximately equal to their rms analysis error, which means the ensemble spreads were reliable overall. Second, we examined whether spread was an accurate predictor of the error for the four individual subsets. Ideally, such spread-skill curve should follow the 45-degree reference line. Fig. 8 shows the result for the surface π norm. The ensemble spreads of both schemes were sub-optimal; they were negatively biased when the analysis error was small and positively biased when the analysis error was large. Such biases were due to the deficiencies of the ensembles generated in each system. In the perfect model experiment conducted here, it was presumably because of the sampling error and the approximations made in estimating the error covariances. The curves for the hybrid and the EnSRF were approximately parallel under the surface π norm (Fig. 8), kinetic energy norm and $\Delta\pi_2$ norm (not shown). This indicated that the ETKF and the EnSRF ensembles had similar skill in estimating the error variance. Results at forecast times e.g., 1-day lead time, were qualitatively the same. Further tests with the

normalized error variance and the kurtosis (Goedicke 1953; Wang and Bishop 2003) of the errors suggested that the abilities of the two systems to distinguish an estimate with large error variance from that with a small error variance were not significantly different.

5. Conclusions and discussions

In this paper, we compared the skill of the hybrid ETKF-3DVAR and the EnSRF analysis schemes in an observing-system simulation experiment under perfect-model assumptions. A two-layer primitive equation global model was used. Each system uses 50-member ensemble. The EnSRF runs provided a reference for the expected analysis accuracy that may be obtained from a state-of-the-art ensemble-based data assimilation method. This assimilation method was costly, however, as it requires parallel assimilation for each member and observations are assimilated serially. In the hybrid ETKF-3DVAR scheme, the flow-dependent covariance from the ETKF was incorporated in the standard 3DVAR when updating the mean state. According to previous work (e.g., Lorenz 2003; Buehner 2005; Barker 1999; Wang et al. 2005), this can be conveniently built as incremental changes to the existing operational variational codes. The ensemble perturbations were updated by the computational efficient ETKF scheme.

Results from this paper demonstrated that the hybrid ETKF-3DVAR achieved a large portion (90%) of the EnSRF's analysis improvement over the 3DVAR. The ability of the ETKF ensemble to estimate the error variance is similar to the EnSRF. Further, the initial conditions of the ETKF-3DVAR are more balanced than those of the EnSRF. The maximal growth in the ETKF ensemble perturbation subspace is larger than that in the EnSRF ensemble perturbation space.

To apply the hybrid scheme in the current operational variational framework where preconditioning with respect to the background term is used, as suggested by Lorenc (2003), Buehner (2005), Barker (1999) and Wang et al. (2005), in the cost function one can add another background term with the extended control variables preconditioned upon the square root of the ensemble covariance. The increment in the observation term is then equal to the weighted sum of the 3DVAR standard increment and that associated with the extended control variables. Experiments with the alpha-extended control variable method (Barker 1999; Dale Barker, personal communication 2005) suggested that with spectral truncation modest extra cost relative to the standard 3DVAR were needed. Observation-space preconditioning, such as the Naval Research Laboratory Atmospheric Variational Data Assimilation System (NAVDAS; Daley and Barker 2001), can also incorporate the ensemble covariance easily by linearly combining the ensemble covariance with the standard 3DVAR covariance.

The idea of the hybrid ETKF-3DVAR may be extended to the 4DVAR framework also. The incorporation of the ensemble covariance may improve its initial background-error covariance estimate and thus improve the 4DVAR analysis. In this case, the ETKF transformation matrix is calculated with observations distributed in both space and time.

Our conclusions about the performance of the hybrid may well be model- and system-dependent. Our implementation of 3DVAR was approximate. For example, in section 3b, covariance localization with scale of 15000km was applied on the limited perturbation samples, which may induce imbalance. The operational 3DVAR, however, is often well designed to maintain the balance. So it is possible that a more carefully

constructed 3DVAR method would perform better, and thus may make the hybrid ETKF-3DVAR analysis even more competitive with or better than the EnSRF. Further, this initial test excluded the effects of model errors, which contaminate operational data assimilations. The 3DVAR covariance in this case not only stabilizes the analysis cycle but also provides a representation of the imperfectly known model error covariance (Etherton and Bishop 2004, Houtekamer et al. 2005). We expect to compare the EnSRF and the hybrid in an imperfect-model framework in future experiments.

Acknowledgements

This research was primarily supported by National Science Foundation grant ATM-0205612. Craig H. Bishop received support under ONR Project Element 0601153N, Project Number BE-033-0345 and also ONR Grant number N00014-00-1-0106.

Appendix A: Derivation of an improved ETKF formulation under the white noise assumption.

Here, we identify gross bias in the ETKF formulation (7) given in Bishop et al. (2001), which occurs when the ensemble size K is significantly less than the rank of the true forecast error covariance r . We shall refer to this version of the ETKF as the “old ETKF”. Having identified and explained the bias, we then give the reasoning behind the bias ameliorated formulation given by equation (8). We believe that this formulation is superior because (a) 1-D simple model experiments (in the forthcoming paper) show that the analysis error variance estimate by formula (8) is closer to an optimal scheme and (b) experiments in this paper also showed that formula (8) delivers superior performance to (7).

The sample background forecast error covariance of a K -member ensemble in the normalized observation space $\tilde{\mathbf{H}}\mathbf{P}^e\tilde{\mathbf{H}}^T$ is given by

$$\tilde{\mathbf{H}}\mathbf{P}^e\tilde{\mathbf{H}}^T = \frac{\sum_{k=1}^K \left(\tilde{\mathbf{H}} \mathbf{x}_k'^b \right) \left(\tilde{\mathbf{H}} \mathbf{x}_k'^b \right)^T}{K-1}, \quad (\text{A.1})$$

where $\tilde{\mathbf{H}}$ is the normalized observation operator, i.e., $\tilde{\mathbf{H}} = \mathbf{R}^{-1/2}\mathbf{H}$, and $\mathbf{x}_k'^b$ is the deviation of the k th member from the ensemble mean. With the innovation-based inflation factor applied (Wang and Bishop 2003), the sample covariance in (A.1) provides a reasonable estimate of the *total* forecast error variance on the *entire* normalized observation space, i.e.,

$$\text{Tr}(\tilde{\mathbf{H}}\mathbf{P}^e\tilde{\mathbf{H}}^T) = \text{Tr}(\mathbf{E}\mathbf{G}\mathbf{E}^T) = \text{Tr}(\mathbf{\Gamma}) = \sum_{j=1}^{K-1} \gamma_j = \text{Tr}(\tilde{\mathbf{H}}\mathbf{P}^f\tilde{\mathbf{H}}^T), \quad (\text{A.2})$$

where Tr is the trace; $\mathbf{E} = [\mathbf{e}_1, \mathbf{e}_2, \dots, \mathbf{e}_j, \dots, \mathbf{e}_{K-1}]$ lists the $K-1$ orthonormal eigenvectors and the diagonal matrix $\mathbf{\Gamma} = diag\{\gamma_1, \gamma_2, \dots, \gamma_j, \dots, \gamma_{K-1}\}$ lists the corresponding non-zero eigenvalues of $\tilde{\mathbf{H}}\mathbf{P}^e\tilde{\mathbf{H}}^T$; $\tilde{\mathbf{H}}\mathbf{P}^f\tilde{\mathbf{H}}^T$ is the true forecast error covariance in normalized observation space. Note that the dimensions of \mathbf{E} , $\mathbf{\Gamma}$, $\tilde{\mathbf{H}}\mathbf{P}^e\tilde{\mathbf{H}}^T$, $\tilde{\mathbf{H}}\mathbf{P}^f\tilde{\mathbf{H}}^T$ are $p \times (K-1)$, $(K-1) \times (K-1)$, $p \times p$, and $p \times p$ respectively, where p is the number of observations.

However, when K is significantly less than r , the sample covariance will generally overestimate the forecast error variance within the vector space spanned by the ensemble perturbations. To see this, we consider the special case where the true forecast error covariance matrix in normalized observation space $\tilde{\mathbf{H}}\mathbf{P}^f\tilde{\mathbf{H}}^T$ has r non-zero eigenvalues all of which have the same value λ , i.e.,

$$\tilde{\mathbf{H}}\mathbf{P}^f\tilde{\mathbf{H}}^T = \mathbf{V}\lambda\mathbf{I}\mathbf{V}^T, \text{ and } \mathbf{V}^T\mathbf{V} = \mathbf{I}. \quad (\text{A.3})$$

where \mathbf{V} is a $p \times r$ matrix and \mathbf{I} is the $r \times r$ identity matrix. Eq. (A.3) defines what we refer to as the *white noise assumption*. From (A.3), $Tr(\tilde{\mathbf{H}}\mathbf{P}^f\tilde{\mathbf{H}}^T) = r\lambda$ and thus from (A.2)

$$\sum_{j=1}^{K-1} \gamma_j = r\lambda \quad (\text{A.4})$$

Eq. (A.4) shows that the sum of all of the r non-zero eigenvalues of the *entire* system is equal to the sum of the $K-1$ eigenvalues γ_j corresponding to the $K-1$ orthogonal eigenvectors of $\tilde{\mathbf{H}}\mathbf{P}^e\tilde{\mathbf{H}}^T$. Note that, in general, $r \gg K$. Note also that the *true* error variance in one of the sample covariance eigenvector directions \mathbf{e}_j is given by

$$\mathbf{e}_j^T \tilde{\mathbf{H}}\mathbf{P}^f\tilde{\mathbf{H}}^T \mathbf{e}_j = \lambda. \quad (\text{A.5})$$

Further from (A.4),

$$\lambda = \frac{\sum_{j=1}^{K-1} \gamma_j}{r} = \frac{(K-1)}{r} \bar{\gamma} \quad (\text{A.6})$$

where $\bar{\gamma} = [1/(K-1)] \sum_{j=1}^{K-1} \gamma_j$ gives the mean of the sample covariance eigenvalues.

Comparison of (A.5) and (A.6) shows that the eigenvalue γ_i overestimates the error variance in the direction associated with its eigenvector by the factor $r/(K-1)$.

Noting that the sample analysis error covariance by the old ETKF (Bishop et al. 2001; Wang and Bishop 2003; Wang et al. 2004) is

$$\tilde{\mathbf{H}} \mathbf{S}^a \tilde{\mathbf{H}}^T = \mathbf{E} \mathbf{\Gamma} (\mathbf{\Gamma} + \mathbf{I})^{-1} \mathbf{E}^T = \sum_{i=1}^{K-1} \mathbf{e}_i \frac{\gamma_i}{\gamma_i + 1} \mathbf{e}_i^T. \quad (\text{A.7})$$

It is evident from (A.7) that the filtering properties of the ETKF error covariance update equation are sensitive to the eigenvalues γ_i . Thus it seems appropriate to replace these eigenvalues by a set of eigenvalues that better reflect the error variance within the ensemble subspace. In other words, it suggests that we replace (A.7) with

$$\tilde{\mathbf{H}} \mathbf{S}^a \tilde{\mathbf{H}}^T = a \mathbf{E} \rho \mathbf{\Gamma} (\rho \mathbf{\Gamma} + \mathbf{I})^{-1} \mathbf{E}^T = a \sum_{i=1}^{K-1} \mathbf{e}_i \frac{\rho \gamma_i}{\rho \gamma_i + 1} \mathbf{e}_i^T. \quad (\text{A.8})$$

The factor ρ in (A.8) gives the percentage of total variance that projects onto the ensemble subspace, i.e.,

$$\rho = \frac{\text{Tr}(\mathbf{E}^T \tilde{\mathbf{H}} \mathbf{P}^f \tilde{\mathbf{H}}^T \mathbf{E})}{\text{Tr}(\tilde{\mathbf{H}} \mathbf{P}^f \tilde{\mathbf{H}}^T)}. \quad (\text{A.9})$$

This choice is motivated by the fact that (A.9) gives

$$\rho = \frac{K-1}{r}, \quad (\text{A.10})$$

which according to the previous discussion is precisely what is required under the white noise assumption. Please refer to Appendix B for how to estimate ρ in (A.9) in general.

The factor a in (A.8) is motivated by the following arguments. While $\mathbf{E} \rho \mathbf{\Gamma} (\rho \mathbf{\Gamma} + \mathbf{I})^{-1} \mathbf{E}^T$ would improve the filtering properties for directions that lie within the ensemble subspace, it does not improve the filtering properties in directions that lie outside the ensemble subspace. We hypothesize that a coefficient a will be required in order to ensure relatively unbiased filtering properties in directions that do not lie entirely within the ensemble perturbation vector subspace. In other words, we search for an a such that the *expected* sample analysis error covariance will give a relatively unbiased estimate of the true analysis error covariance, $\tilde{\mathbf{H}} \mathbf{P}^a \tilde{\mathbf{H}}^T$, i.e.,

$$\tilde{\mathbf{H}} \mathbf{P}^a \tilde{\mathbf{H}}^T = \langle \tilde{\mathbf{H}} \mathbf{S}^a \tilde{\mathbf{H}}^T \rangle = a \left\langle \sum_{j=1}^{K-1} \mathbf{e}_j \frac{\rho \gamma_j}{\rho \gamma_j + 1} \mathbf{e}_j^T \right\rangle, \quad (\text{A.11})$$

In (A.11) the angle bracket on the far right side of (A.11) represents the average over an infinite number of independent calculations of $\mathbf{E} \rho \mathbf{\Gamma} (\rho \mathbf{\Gamma} + \mathbf{I})^{-1} \mathbf{E}^T$ obtained from a corresponding infinite number of independent K -member ensembles.

Next we choose a so that it satisfies (A.11) under the white spectrum assumption. Under this assumption, the true analysis error covariance is (Wang and Bishop 2003)

$$\tilde{\mathbf{H}} \mathbf{P}^a \tilde{\mathbf{H}}^T = \mathbf{V} \lambda / (\lambda + 1) \mathbf{I} \mathbf{V}^T = \sum_{i=1}^r \mathbf{v}_i \frac{\lambda}{\lambda + 1} \mathbf{v}_i^T. \quad (\text{A.12})$$

Substituting (A.12) into (A.11), premultiplying by \mathbf{v}_i^T and postmultiplying by \mathbf{v}_i one obtains

$$\begin{aligned}
\frac{\lambda}{\lambda+1} &= a \left\langle \mathbf{v}_i^T \left(\sum_{j=1}^{K-1} \mathbf{e}_j \frac{\rho\gamma_j}{\rho\gamma_j+1} \mathbf{e}_j^T \right) \mathbf{v}_i \right\rangle \\
&= a \left\langle \sum_{j=1}^{K-1} \left(\frac{\rho\gamma_j}{\rho\gamma_j+1} \right) \mathbf{v}_i^T \mathbf{e}_j \mathbf{e}_j^T \mathbf{v}_i \right\rangle.
\end{aligned} \tag{A.13}$$

Note that the term $\mathbf{v}_i^T \mathbf{e}_j \mathbf{e}_j^T \mathbf{v}_i$ represents the square of the projection of the i th true eigenvector on the j th sample covariance eigenvector. Under the white noise approximation, variations in this term are uncorrelated with variations in γ_j and hence (A.13) can be rewritten in the form,

$$\frac{\lambda}{\lambda+1} = a \sum_{j=1}^{K-1} \left\langle \left(\frac{\rho\gamma_j}{\rho\gamma_j+1} \right) \right\rangle \langle \mathbf{v}_i^T \mathbf{e}_j \mathbf{e}_j^T \mathbf{v}_i \rangle. \tag{A.14}$$

Also, the direction \mathbf{e}_m is statistically interchangeable with the direction \mathbf{e}_n under the white noise assumption. Hence $\langle \mathbf{v}_i^T \mathbf{e}_j \mathbf{e}_j^T \mathbf{v}_i \rangle$ and $\left\langle \left(\frac{\rho\gamma_j}{\rho\gamma_j+1} \right) \right\rangle$ have the same value for all j . Furthermore, note that we could easily augment the $K-1$ orthonormal basis \mathbf{E} using Gram-Schmidt orthogonalization (Golub and Van Loan, 1989) to obtain an expanded r -dimensional subspace \mathbf{E}^E that precisely spanned the same space of the true eigenvectors \mathbf{V} . Hence,

$$\left\langle \mathbf{v}_i^T \mathbf{E}^E (\mathbf{E}^E)^T \mathbf{v}_i \right\rangle = 1 = \sum_{j=1}^r \langle \mathbf{v}_i^T \mathbf{e}_j \mathbf{e}_j^T \mathbf{v}_i \rangle = r \langle \mathbf{v}_i^T \mathbf{e}_j \mathbf{e}_j^T \mathbf{v}_i \rangle \tag{A.15}$$

Eq. (A.15) implies that

$$\langle \mathbf{v}_i^T \mathbf{e}_j \mathbf{e}_j^T \mathbf{v}_i \rangle = \frac{1}{r} \tag{A.16}$$

Further under the white noise assumption, we assume that γ_j is close to $\bar{\gamma}$. Thus from

(A.6) and (A.10), $\rho\gamma_j \approx \lambda$, which leads to

$$\frac{\lambda}{\lambda + 1} \approx \left\langle \left(\frac{\rho\gamma_j}{\rho\gamma_j + 1} \right) \right\rangle \quad (\text{A.17})$$

Using (A.17) and (A.16) in (A.15) then gives

$$a \approx \frac{r}{K-1} = \frac{1}{\rho}. \quad (\text{A.18})$$

Note from (A.16), $\frac{1}{a} \approx \frac{K-1}{r} = \rho$ is the expected squared projection of a true eigenvector

onto $K-1$ ensemble based eigenvectors. It is directly related to the expected angle

subtended between ensemble eigenvectors and true eigenvectors. Using (A.18) in (A.11)

suggests that if we define the sample analysis error covariance as

$$\tilde{\mathbf{H}}\mathbf{S}^a\tilde{\mathbf{H}}^T = \mathbf{E}\mathbf{\Gamma}(\rho\mathbf{\Gamma}+\mathbf{I})^{-1}\mathbf{E} = \sum_{j=1}^{K-1} \mathbf{e}_j \frac{\gamma_j}{\rho\gamma_j + 1} \mathbf{e}_j^T, \quad (\text{A.19})$$

the *expected* value of it will provide a less biased estimate of the true analysis error

covariance $\tilde{\mathbf{H}}\mathbf{P}^a\tilde{\mathbf{H}}^T$ than the old ETKF. From (10), the sample analysis error covariance

in state space that is consistent with (A.19) is

$$\mathbf{S}^a = \mathbf{X}^b\mathbf{C}(\rho\mathbf{\Gamma}+\mathbf{I})^{-1}\mathbf{C}^T(\mathbf{X}^b)^T / (K-1). \quad (\text{A.20})$$

Thus, the new transformation matrix given by (8) is recovered.

Appendix B: Estimating the ρ parameter in (A.9)

To estimate the ρ factor in (A.9), we need to estimate the total forecast error

variance in normalized observation space $Tr(\tilde{\mathbf{H}}\mathbf{P}^f\tilde{\mathbf{H}}^T)$ and its projection onto the

ensemble subspace $Tr(\mathbf{E}^T \tilde{\mathbf{H}} \mathbf{P}^f \tilde{\mathbf{H}}^T \mathbf{E})$. The difference between observation and forecast vectors, i.e., the innovations, enables both of these tasks.

First, note that since

$$\begin{aligned} Tr(\tilde{\mathbf{H}} \mathbf{P}^f \tilde{\mathbf{H}}^T + \mathbf{I}) &= Tr \left\langle \left[\mathbf{R}^{-1/2} \mathbf{y} - \tilde{\mathbf{H}} \bar{\mathbf{x}}^b \right] \left[\mathbf{R}^{-1/2} \mathbf{y} - \tilde{\mathbf{H}} \bar{\mathbf{x}}^b \right]^T \right\rangle \\ &= \left\langle \left[\mathbf{R}^{-1/2} \mathbf{y} - \tilde{\mathbf{H}} \bar{\mathbf{x}}^b \right]^T \left[\mathbf{R}^{-1/2} \mathbf{y} - \tilde{\mathbf{H}} \bar{\mathbf{x}}^b \right] \right\rangle. \end{aligned} \quad (\text{B.1})$$

It follows that the approximation

$$Tr(\tilde{\mathbf{H}} \mathbf{P}^f \tilde{\mathbf{H}}^T) \approx \left[\mathbf{R}^{-1/2} \mathbf{y} - \tilde{\mathbf{H}} \bar{\mathbf{x}}^b \right]^T \left[\mathbf{R}^{-1/2} \mathbf{y} - \tilde{\mathbf{H}} \bar{\mathbf{x}}^b \right] - p, \quad (\text{B.2})$$

where p is the number of observations, gives an unbiased estimate of the trace of the total forecast error variance in normalized observation space. To estimate the accuracy of the approximation (B.2), recognize that

$$\mathbf{R}^{-1/2} \mathbf{y} - \tilde{\mathbf{H}} \bar{\mathbf{x}}^b = \sum_{i=1}^p \eta_i \mathbf{v}_i, \quad (\text{B.3})$$

where \mathbf{v}_i is the i th eigenvector of the normalized innovation covariance $\tilde{\mathbf{H}} \mathbf{P}^f \tilde{\mathbf{H}}^T + \mathbf{I}$ and η_i is a random variable with mean zero and variance equal to the i th eigenvalue σ_i of $\tilde{\mathbf{H}} \mathbf{P}^f \tilde{\mathbf{H}}^T + \mathbf{I}$. Eq. (B.3) implies that

$$\frac{\left[\mathbf{R}^{-1/2} \mathbf{y} - \tilde{\mathbf{H}} \bar{\mathbf{x}}^b \right]^T \left[\mathbf{R}^{-1/2} \mathbf{y} - \tilde{\mathbf{H}} \bar{\mathbf{x}}^b \right]}{\left\langle \left[\mathbf{R}^{-1/2} \mathbf{y} - \tilde{\mathbf{H}} \bar{\mathbf{x}}^b \right]^T \left[\mathbf{R}^{-1/2} \mathbf{y} - \tilde{\mathbf{H}} \bar{\mathbf{x}}^b \right] \right\rangle} = \frac{\sum_{i=1}^p \eta_i^2}{\sum_{i=1}^p \sigma_i} = \frac{\sum_{i=1}^p \eta_i^2}{p \bar{\sigma}}. \quad (\text{B.4})$$

Note that if the eigenspectrum of $\tilde{\mathbf{H}} \mathbf{P}^f \tilde{\mathbf{H}}^T + \mathbf{I}$ were flat (white) with $\sigma_i = \text{constant}$ for all i , and η_i is normally distributed, then the numerator of (B.4) would be a χ^2 variable with p degrees of freedom (Ross 1998, p267). Hence, in this case, (B.4) tends to unity as p

tends to infinity. Tables of χ^2 statistics can be used to determine the reliability of estimates obtained through (B.2).

In typical atmospheric and oceanographic applications, however, little is known about the eigenvalue spectrum of the innovation covariance matrix. In such cases, the only meaningful test of the accuracy of (B.2) is to check the variance of a sample of squared innovations. Since (B.2) is an unbiased estimate, small variance is indicative of estimation accuracy. Wang and Bishop's (2003) experience in using (B.2) to generate an inflation factor for an old-ETKF ensemble in a low resolution (T42) global circulation model suggests that, for the atmosphere, the innovation associated with the global rawinsonde network has enough degrees of freedom to make (B.2) useful. If the observational network is sparse, assuming that the distributions from which

$\left[\mathbf{R}^{-1/2} \mathbf{y} - \tilde{\mathbf{H}} \bar{\mathbf{x}}^b \right]^T \left[\mathbf{R}^{-1/2} \mathbf{y} - \tilde{\mathbf{H}} \bar{\mathbf{x}}^b \right]$ are sampled have a degree of time invariance, then the approximation

$$Tr(\tilde{\mathbf{H}} \mathbf{P}^f \tilde{\mathbf{H}}^T) \approx \overline{\left[\mathbf{R}^{-1/2} \mathbf{y} - \tilde{\mathbf{H}} \bar{\mathbf{x}}^b \right]^T \left[\mathbf{R}^{-1/2} \mathbf{y} - \tilde{\mathbf{H}} \bar{\mathbf{x}}^b \right]} - p, \quad (\text{B.5})$$

can be used. The overbar in (B.5) represents the average of

$\left[\mathbf{R}^{-1/2} \mathbf{y} - \tilde{\mathbf{H}} \bar{\mathbf{x}}^b \right]^T \left[\mathbf{R}^{-1/2} \mathbf{y} - \tilde{\mathbf{H}} \bar{\mathbf{x}}^b \right]$ computed over a period of time.

Having obtained a plausible estimate of $Tr(\tilde{\mathbf{H}} \mathbf{P}^f \tilde{\mathbf{H}}^T)$, one also needs to estimate $Tr(\mathbf{E}^T \tilde{\mathbf{H}} \mathbf{P}^f \tilde{\mathbf{H}}^T \mathbf{E})$. Replacing $\tilde{\mathbf{H}} \mathbf{P}^f \tilde{\mathbf{H}}^T + \mathbf{I}$ by $\mathbf{E}^T (\tilde{\mathbf{H}} \mathbf{P}^f \tilde{\mathbf{H}}^T + \mathbf{I}) \mathbf{E}$ in (B.1), leads to the approximation

$$Tr(\mathbf{E}^T \tilde{\mathbf{H}} \mathbf{P}^f \tilde{\mathbf{H}}^T \mathbf{E}) \approx \left[\mathbf{R}^{-1/2} \mathbf{y} - \tilde{\mathbf{H}} \bar{\mathbf{x}}^b \right]^T \mathbf{E} \mathbf{E}^T \left[\mathbf{R}^{-1/2} \mathbf{y} - \tilde{\mathbf{H}} \bar{\mathbf{x}}^b \right] - (K-1), \quad (\text{B.6})$$

and the $\mathbf{E}^T (\tilde{\mathbf{H}} \mathbf{P}^f \tilde{\mathbf{H}}^T + \mathbf{I}) \mathbf{E}$ counterpart of (B.4) is

$$\frac{\left[\mathbf{R}^{-1/2} \mathbf{y} - \tilde{\mathbf{H}} \bar{\mathbf{x}}^b \right]^T \mathbf{E} \mathbf{E}^T \left[\mathbf{R}^{-1/2} \mathbf{y} - \tilde{\mathbf{H}} \bar{\mathbf{x}}^b \right]}{\left\langle \left[\mathbf{R}^{-1/2} \mathbf{y} - \tilde{\mathbf{H}} \bar{\mathbf{x}}^b \right]^T \mathbf{E} \mathbf{E}^T \left[\mathbf{R}^{-1/2} \mathbf{y} - \tilde{\mathbf{H}} \bar{\mathbf{x}}^b \right] \right\rangle} = \frac{\sum_{i=1}^{K-1} \xi_i^2}{\sum_{i=1}^{K-1} v_i} = \frac{\sum_{i=1}^{K-1} \xi_i^2}{(K-1)\bar{v}}, \quad (\text{B.7})$$

where v_i is the i th eigenvalue of the $(K-1) \times (K-1)$ normalized innovation covariance

$\mathbf{E}^T (\tilde{\mathbf{H}} \mathbf{P}^f \tilde{\mathbf{H}}^T + \mathbf{I}) \mathbf{E}$, ξ_i is a random variable with mean zero and variance v_i . In (B.7) \bar{v}

gives the mean of the eigenvalues.

From our previous discussion of (B.2) and (B.4), large ensemble sizes K would generally be required in order to give (B.6) a high level of accuracy. If only a small ensemble is available, similarly to (B.5), the approximation

$$\text{Tr}(\mathbf{E}^T \tilde{\mathbf{H}} \mathbf{P}^f \tilde{\mathbf{H}}^T \mathbf{E}) \approx \overline{\left[\mathbf{R}^{-1/2} \mathbf{y} - \tilde{\mathbf{H}} \bar{\mathbf{x}}^b \right]^T \mathbf{E} \mathbf{E}^T \left[\mathbf{R}^{-1/2} \mathbf{y} - \tilde{\mathbf{H}} \bar{\mathbf{x}}^b \right]} - (K-1), \quad (\text{B.8})$$

can be used. Given (B.5) and (B.8), the estimated ρ factor is given by (9). In the current experiment, the overbars in (B.5) and (B.8) are the average of the two weeks of data previous to the current time.

References

- Anderson, J. L., 2001: An ensemble adjustment Kalman filter for data assimilation. *Mon. Wea. Rev.*, **129**, 2884-2903.
- Barker, D. M., 1999: Var scientific development paper 25: The use of synoptically-dependent error structures in 3DVAR. UK MET office technical report, available at dmbarker@ucar.edu.
- Bishop, C. H., and Z. Toth, 1999: Ensemble transformation and adaptive observations. *J. Atmos. Sci.*, **56**, 1748-1765.
- , B. J. Etherton, and S. J. Majumdar, 2001: Adaptive sampling with the ensemble transform Kalman filter. Part I: Theoretical Aspects. *Mon. Wea. Rev.*, **129**, 420-436.
- Buehner, M., 2005: Ensemble-derived stationary and flow-dependent background-error covariances: evaluation in a quasi-operational NWP setting. *Quart. J. Roy. Meteor. Soc.*, **131**, 1013-1043.
- Burgers, G., P. J. van Leeuwen, and G. Evensen, 1998: Analysis scheme in the ensemble Kalman filter. *Mon. Wea. Rev.*, **126**, 1719-1724.
- Cohn, S. E., D. M. da Silva, J. Guo, M. Sienkiewicz and D. Lamich, 1998: Assessing the effects of data selection with the DAO physical space statistical analysis system. *Mon. Wea. Rev.*, **126**, 2913-2926.
- Courtier, P., J. N. Thepaut, and A. Hollingsworth, 1994: A strategy for operational implementation of 4D-VAR, using an incremental approach. *Quart. J. Roy. Meteor. Soc.*, **120**, 1367-1387.

- , E. Andersson, W. Heckley, J. Pailleux, D. Vasiljevic, J. Hamrud, A. Hollingsworth, F. Rabier, and M. Fisher, 1998: The ECMWF implementation of three-dimensional variational assimilation (3D-Var). I: Formulation. *Quart. J. Roy. Meteor. Soc.*, **124**, 1783-1807.
- Daley, R., 1991: *Atmospheric Data Analysis*. Cambridge University Press, 457 pp.
- Dee, D. P., 1995: On-line estimation of error covariance parameters for atmospheric data assimilation. *Mon. Wea. Rev.*, **123**, 1128-1196.
- Etherton, B. J. and C. H. Bishop, 2004: Resilience of hybrid ensemble/3DVAR analysis schemes to model error and ensemble covariance error. *Mon. Wea. Rev.*, **132**, 1065-1080.
- Evensen, G., 1994: Sequential data assimilation with a nonlinear quasigeostrophic model using Monte Carlo methods to forecast error statistics. *J. Geophys. Res.*, **99(C5)**, 10143-10162.
- , 2003: The ensemble Kalman filter: theoretical formulation and practical implementation. *Ocean Dynamics*, **53**, 343-367.
- Gaspari, G. and S. E. Cohn, 1999: Construction of correlation functions in two and three dimensions. *Quart. J. Roy. Meteor. Soc.*, **125**, 723-757.
- Gauthier, P. C., L. Churette, L. Fillion, P. Koclas, and S. Laroche, 1998: Implementation of a 3D variational data assimilation system at the Canadian Meteorological Center. Part I: The global analysis. *Atmos. Ocean*, **37**, 103-156.
- Geodicke, V. A., 1953: *Introduction to the theory of statistics*. Academic Press, 286pp.
- Golub, G. H. and C. F. Van Loan, 1989: *Matrix computations*. The John Hopkins University Press, 642pp.

- Hamill, T. M., C. Snyder, and R. E. Morss, 2000: A comparison of probabilistic forecast from bred, singular vector, and perturbed observation ensembles. *Mon. Wea. Rev.*, **128**, 1835-1851.
- and C. Snyder, 2000: A hybrid ensemble Kalman filter-3D variational analysis scheme. *Mon. Wea. Rev.*, **128**, 2905-2919.
- , J. S. Whitaker, and C. Snyder, 2001: Distance-dependent filtering of background error covariance estimates in an ensemble Kalman filter. *Mon. Wea. Rev.*, **129**, 2776-2790.
- , and —, 2005: Accounting for the error due to unresolved scales in ensemble data assimilation: a comparison of different approaches *Mon. Wea. Rev.*, in press.
Available at http://www.cdc.noaa.gov/people/tom.hamill/modelerr_v3.pdf
- , 2005: Ensemble based atmospheric data assimilation. To appear in *Predictability of Weather and Climate*, R. Hagedorn and T. N. Palmer, eds. Cambridge Press. Available at
www.cdc.noaa.gov/people/tom.hamill/efda_review5.pdf
- Houtekamer, P. L., and H. L. Mitchell, 1998: Data assimilation using an ensemble Kalman filter technique. *Mon. Wea. Rev.*, **126**, 796-811.
- , and —, 2001: A sequential ensemble Kalman filter for atmospheric data assimilation. *Mon. Wea. Rev.*, **129**, 123-137.
- , —, G. Pellerin, M. Buehner and M. Charron, 2005: Atmospheric data assimilation with an ensemble Kalman filter: results with real observations. *Mon. Wea. Rev.*, **133**, 604-620.

- , and —, 2005: Ensemble Kalman filtering. *Quart. J. Roy. Meteor. Soc.*, submitted.
Available from Peter.Houtekamer@ec.gc.ca
- Liu, H., M. Xue, J. R. Purser, and D. F. Parrish, 2005: Retrieval of moisture from GPS slant-path water vapor observations using 3DVAR with isotropic and anisotropic recursive filters. *Preprints, 17th conference on numerical weather prediction*, Washington DC. Available at
http://ams.confex.com/ams/WAFNWP34BC/techprogram/paper_94296.htm
- Lorenc, A. C., 2003: The potential of the ensemble Kalman filter for NWP – a comparison with 4D-VAR. *Quart. J. Roy. Meteor. Soc.*, **129**, 3183-3203.
- Lynch, P. and X.-Y. Huang, 1992: Initialization of the HIRLAM model using a digital filter. *Mon. Wea. Rev.*, **120**, 1019-1034.
- Majumdar, S. J., C. H. Bishop, B. J. Etherton, I. Szunyogh, Z. Toth, 2001: Can an ensemble transform Kalman filter predict the reduction in forecast-error variance produced by targeted observations?
- , —, —, and Z. Toth. 2002a: Adaptive sampling with the ensemble transform Kalman filter. Part II: field program implementation. *Mon. Wea. Rev.*, **130**, 1356–1369.
- , —, R. Buizza and R. Gelaro, 2002b: A comparison of ensemble transform Kalman filter targeting guidance with ECMWF and NRL total-energy singular vector guidance. *Quart. J. Roy. Meteor. Soc.*, **128**, 2527-2549.
- Mitchell, H. L., P. L. Houtekamer, and G. Pellerin, 2002: Ensemble size, balance, and model-error representation in an ensemble Kalman filter. *Mon. Wea. Rev.*, **130**, 2791-2808.

- Ott, E., B. R. Hunt, I. Szunyogh, A. V. Zimin, E. J. Kostelich, J. Corazza, E. Kalnay, D. J. Patil and J. A. Yorke, 2004: A local ensemble Kalman filter for atmospheric data assimilation. *Tellus*, **56 A**, 415-428.
- Parrish, D. F., and J. C. Derber, 1992: The National Meteorological Center's spectral statistical interpolation analysis system. *Mon. Wea. Rev.*, **120**, 1747-1763.
- Purser, J.R., W.S. Wu, D. F. Parrish and N. M. Roberts, 2003: Numerical aspects of the application of recursive filters to variational statistical analysis. Part II: spatially inhomogeneous and anisotropic general covariances. *Mon. Wea. Rev.*, **131**, 1536-1548.
- Rabier, F., J. N. Thepaut, and P. Courtier, 1998: Extended assimilation and forecast experiments with a four-dimensional variational assimilation system. *Quart. J. Roy. Meteor. Soc.*, **124**, 1-39.
- , H. Jarvinen, E. Klinker, J. F. Mahfouf, and A. Simmons, 2000: The ECMWF operational implementation of four-dimensional variational assimilation. I: experimental results with simplified physics. *Quart. J. Roy. Meteor. Soc.*, **126**, 1143-1170.
- Riishøjgaard, L.-P., 1998: A direct way of specifying flow-dependent background error correlations for meteorological analysis systems. *Tellus*, **50A**, 42–57.
- Ross, Sheldon, 1998: *A First Course in Probability*. Prentice Hall, 514pp
- Snyder, C., and F. Zhang, 2003: Assimilation of simulated Doppler radar observations with an ensemble Kalman filter. *Mon. Wea. Rev.*, **131**, 1663-1677.

- Szunyogh, I., E. J. Kostelich, G. Gyarmati, D. J. Patil, B. R. Hunt, E. Kalnay, E. Ott and J. A. York 2005: Assessing a local ensemble Kalman filter: perfect model experiments with the NCEP global model. *Tellus*, **57A**, in press.
- Tippett, M. K., J. L. Anderson, C. H. Bishop, T. M. Hamill, and J. S. Whitaker, 2003: Ensemble square root filters. *Mon. Wea. Rev.*, **131**, 1485-1490.
- Tong, M. and X. Ming, 2005: Ensemble Kalman filter assimilation of Doppler radar data with a compressible nonhydrostatic model: OSS experiments. *Mon. Wea. Rev.*, **133**, 1789-1807.
- Toth, Z., and E. Kalnay, 1993: Ensemble forecasting at NMC: The generation of perturbations. *Bull. Amer. Meteor. Soc.*, **74**, 2317-2330.
- , and —, 1997: Ensemble forecasting at NCEP and the breeding method. *Mon. Wea. Rev.*, **125**, 3297-3319.
- Wang, X. C. H. Bishop, 2003: A comparison of breeding and ensemble transform Kalman filter ensemble forecast schemes. *J. Atmos. Sci.*, **60**, 1140-1158.
- , —, and S.J. Julier, 2004: Which is better, an ensemble of positive-negative pairs or a centered spherical simplex ensemble? *Mon. Wea. Rev.*, **132**, 1590-1605.
- , C. Snyder, and T.M. Hamill, 2005: On the theoretical equivalence of differently proposed ensemble/3D-Var hybrid analysis schemes. Submitted to *Mon. Wea. Rev.*, available at xuguang.wang@noaa.gov
- Whitaker, J. S. and T. M. Hamill, 2002: Ensemble data assimilation without perturbed observations. *Mon. Wea. Rev.*, **130**, 1913-1924.

- and —, 2005: Ensemble data assimilation with the NCEP GFS model. *Preprints, 17th conference on numerical weather prediction*, Washington DC. Available at Jeffrey.s.Whitaker@noaa.gov.
- Wu, W.S., J. R. Purser, and D. F. Parrish. 2002: Three-dimensional variational analysis with spatially inhomogeneous covariances. *Mon. Wea. Rev.*, **130**, 2905-2916.
- Zhang, S. and J. L. Anderson, 2003: Impact of spatially and temporally varying estimates of error covariance on assimilation in a simple atmospheric model. *Tellus*, 55A, 126-147.
- Zhang, F., C. Snyder and J. Sun, 2004: Impacts of initial estimate and observation availability on convective-scale data assimilation with an ensemble Kalman filter. *Mon. Wea. Rev.*, **132**, 1238-1253.
- Zou, X., A. Barcilon, I. M. Navon, J. Whitaker, and D. G. Cacuci, 1993: An adjoint sensitivity study of blocking in a two-layer isentropic model. *Mon. Wea. Rev.*, **121**, 2833-2857.

Figure captions

Fig. 1. Illustration of the hybrid ETKF-3DVAR analysis and ensemble generation cycle for a hypothetical three-member ensemble. The ensemble mean is updated with the background-error covariance estimated by the linear combination of the ETKF ensemble covariance and the 3DVAR covariance. The ensemble perturbation is updated by the ETKF transformation matrix with innovation based inflation applied.

Fig. 2. Observation locations on 362 spherical geodesic grids.

Fig. 3 Root-mean square analysis error for kinetic-energy norm, upper-layer thickness $\Delta\pi_2$ norm, and surface π norm. The black bars are results for the hybrid ETKF-3DVAR scheme with different linear combination coefficients $\alpha = 0.2, 0.4, 0.6, 0.8$, and 1.0 . The grey bars are results for the EnSRF with different covariance localization scales of 5000 km, 15000 km, 25000 km, 35000 km, and 45000 km. The white bar is for the 3DVAR.

Fig. 4. A snapshot (at the 100th analysis cycle) of the ensemble mean upper layer wind (U , V) and thickness ($\Delta\pi_2$) increments for single $-3 J kg^{-1} K^{-1}$ $\Delta\pi_2$ observation increment for the ETKF-3DVAR scheme with $\alpha = 0.4$. The black dot is the observation location. The contours and color shades are the background ensemble mean and the analysis increment at the 100th cycle for (a) upper layer U wind, (b) upper layer V wind, and (c) upper layer thickness $\Delta\pi_2$. The contour intervals for the background mean are from $-20 ms^{-1}$ to $45 ms^{-1}$ by $5 ms^{-1}$ for (a), from $-24 ms^{-1}$ to $28 ms^{-1}$ by $4 ms^{-1}$ for (b) and from $75 J kg^{-1} K^{-1}$ to $450 J kg^{-1} K^{-1}$ by $25 J kg^{-1} K^{-1}$.

Fig. 5. Same as Fig. 4, except for the EnSRF with localization scale of 25000km.

Fig. 6. Maximal 24-h perturbation growth in global kinetic-energy norm within the ensemble perturbation subspace for the hybrid ETKF-3DVAR (black bars), with different linear combination coefficients $\alpha = 0.2, 0.4, 0.6, 0.8$, and 1.0 , and the EnSRF (grey bars) with different covariance localization scales (5000km, 15000km, 25000km, 35000km, and 45000km).

Fig. 7. Mean absolute surface π tendency ($\text{J kg}^{-1} \text{K}^{-1} \text{h}^{-1}$) averaged globally, over the subsequent 23 1-h forecast periods and over all ensemble members. The black bars are for the hybrid ETKF-3DVAR with different linear combination coefficients $\alpha = 0.2, 0.4, 0.6, 0.8$, and 1.0 , and the grey bars are for the EnSRF with different covariance localization scales (5000 km, 15000 km, 25000 km, 35000 km, and 45000 km). The white is for the truth.

Fig. 8. The relationship between the surface π analysis spread and rms analysis error for the hybrid ETKF-3DVAR (dashed) and the EnSRF (solid). The dotted line is a reference line for a perfect ensemble.

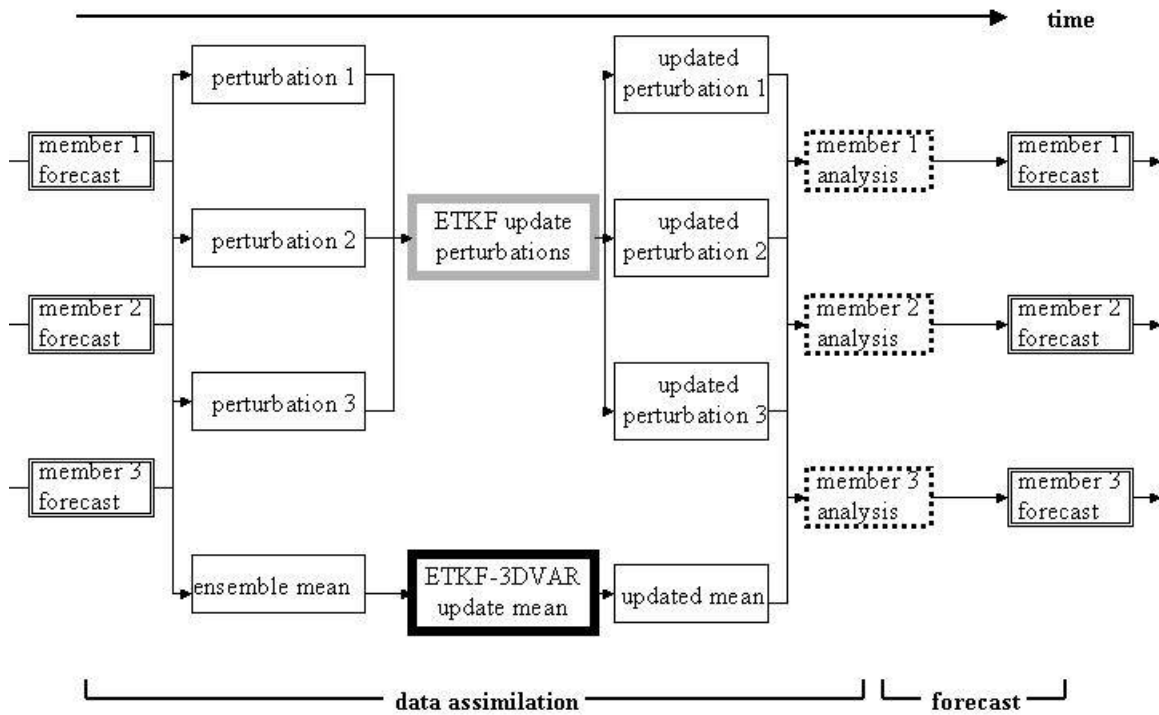


Figure 1. Illustration of the hybrid ETKF-3DVAR analysis and ensemble generation cycle for a hypothetical three-member ensemble. The ensemble mean is updated with the background-error covariance estimated by the linear combination of the ETKF ensemble covariance and the 3DVAR covariance. The ensemble perturbation is updated by the ETKF transformation matrix with innovation based inflation applied.

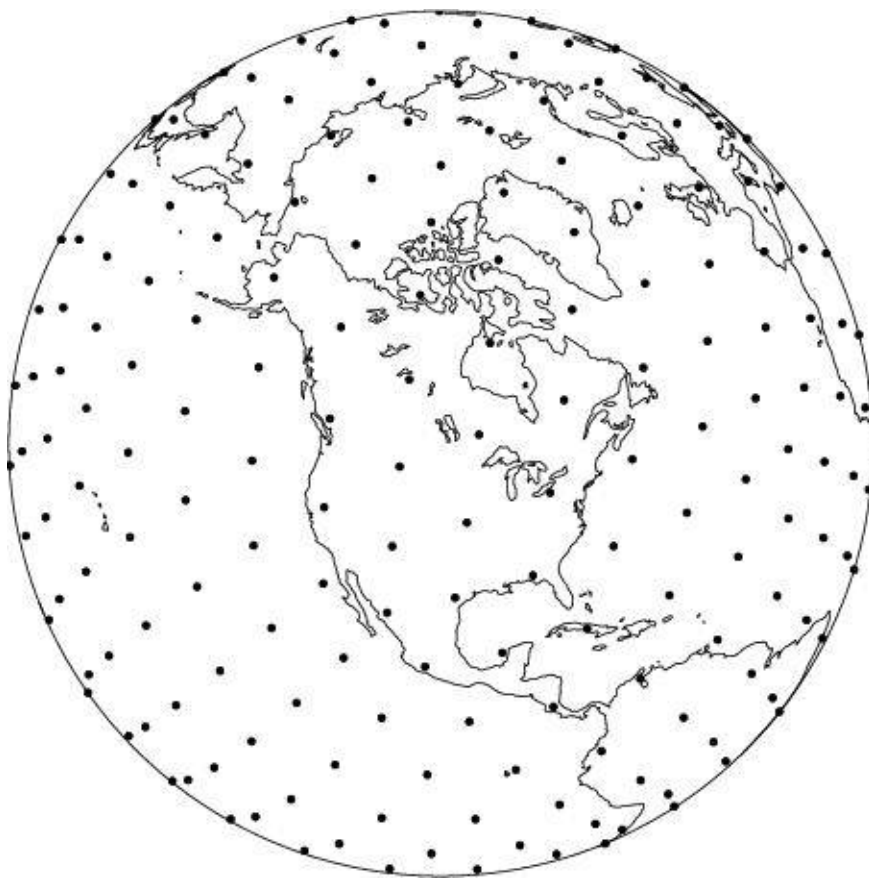


Fig. 2 Observation locations on 362 spherical geodesic grids.

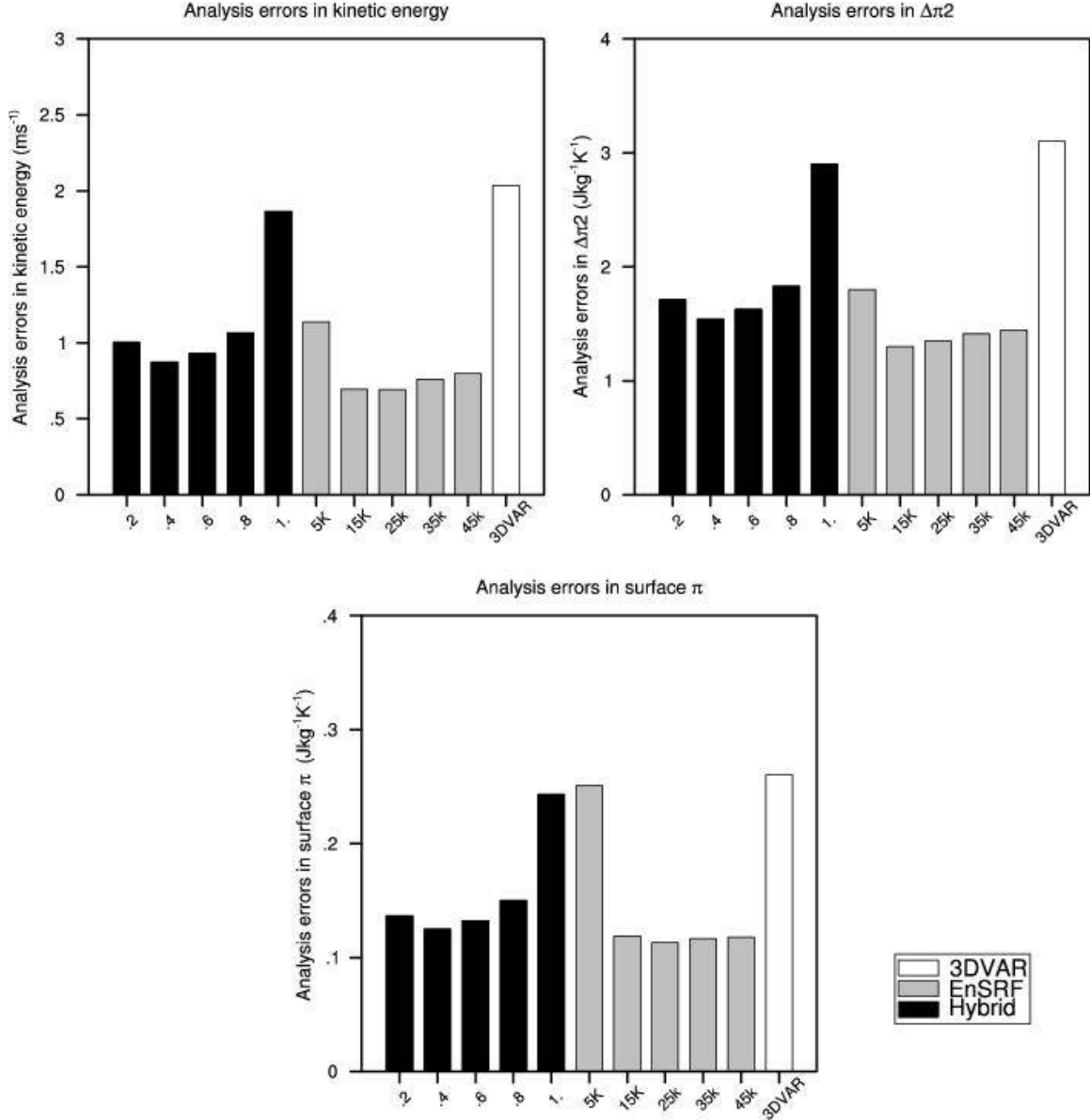


Fig. 3: Root-mean square analysis error for kinetic-energy norm, upper-layer thickness $\Delta\pi_2$ norm, and surface π norm. The black bars are results for the hybrid ETKF-3DVAR scheme with different linear combination coefficients $\alpha = 0.2, 0.4, 0.6, 0.8$, and 1.0 . The grey bars are results for the EnSRF with different covariance localization scales of 5000 km, 15000 km, 25000 km, 35000 km, and 45000 km. The white bar is for the 3DVAR.

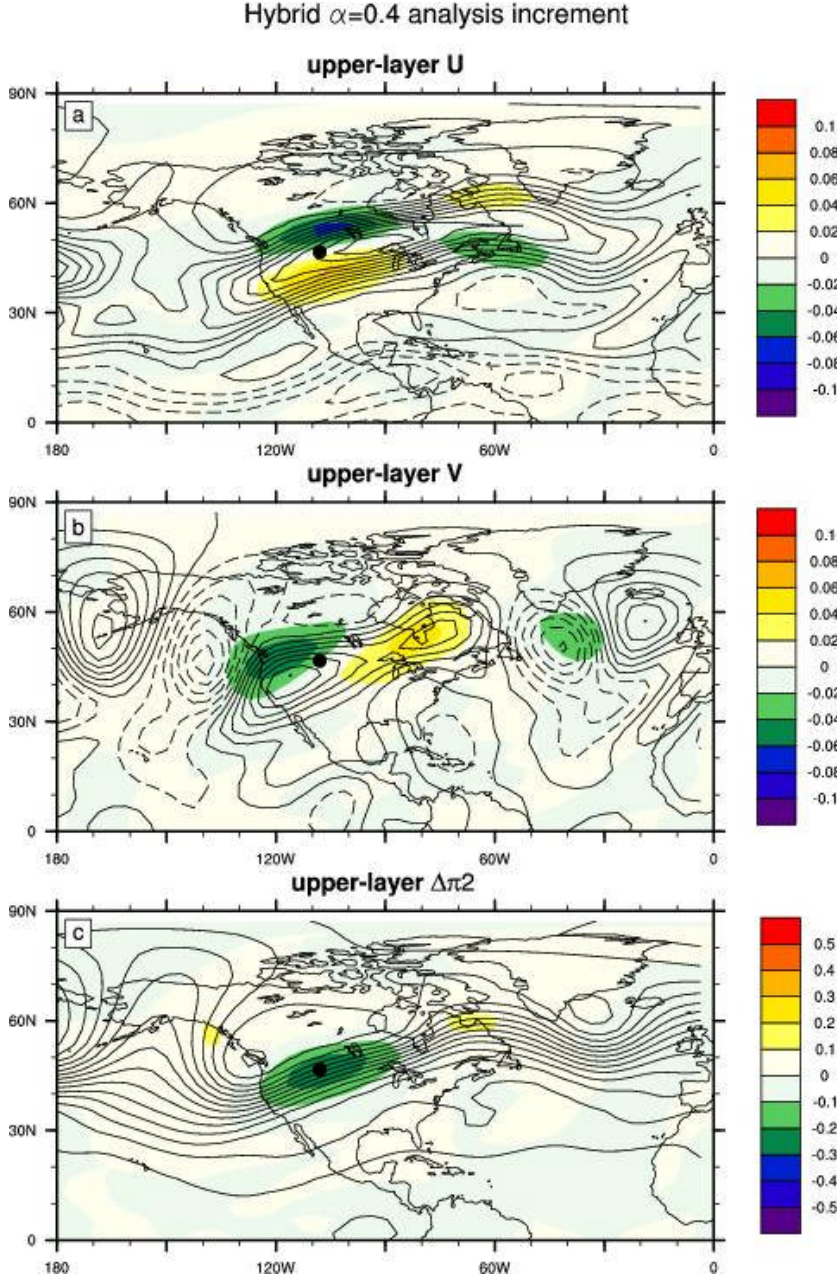


Fig. 4: A snapshot (at the 100th analysis cycle) of the ensemble mean upper layer wind (U , V) and thickness ($\Delta\pi_2$) increments for single $-3 \text{ J kg}^{-1} \text{ K}^{-1}$ $\Delta\pi_2$ observation increment for the ETKF-3DVAR scheme with $\alpha = 0.4$. The black dot is the observation location. The contours and color shades are the background ensemble mean and the analysis increment at the 100th cycle for (a) upper layer U wind, (b) upper layer V wind, and (c) upper layer thickness $\Delta\pi_2$. The contour intervals for the background mean are from -20 ms^{-1} to 45 ms^{-1} by 5 ms^{-1} for (a), from -24 ms^{-1} to 28 ms^{-1} by 4 ms^{-1} for (b) and from $75 \text{ J kg}^{-1} \text{ K}^{-1}$ to $450 \text{ J kg}^{-1} \text{ K}^{-1}$ by $25 \text{ J kg}^{-1} \text{ K}^{-1}$.

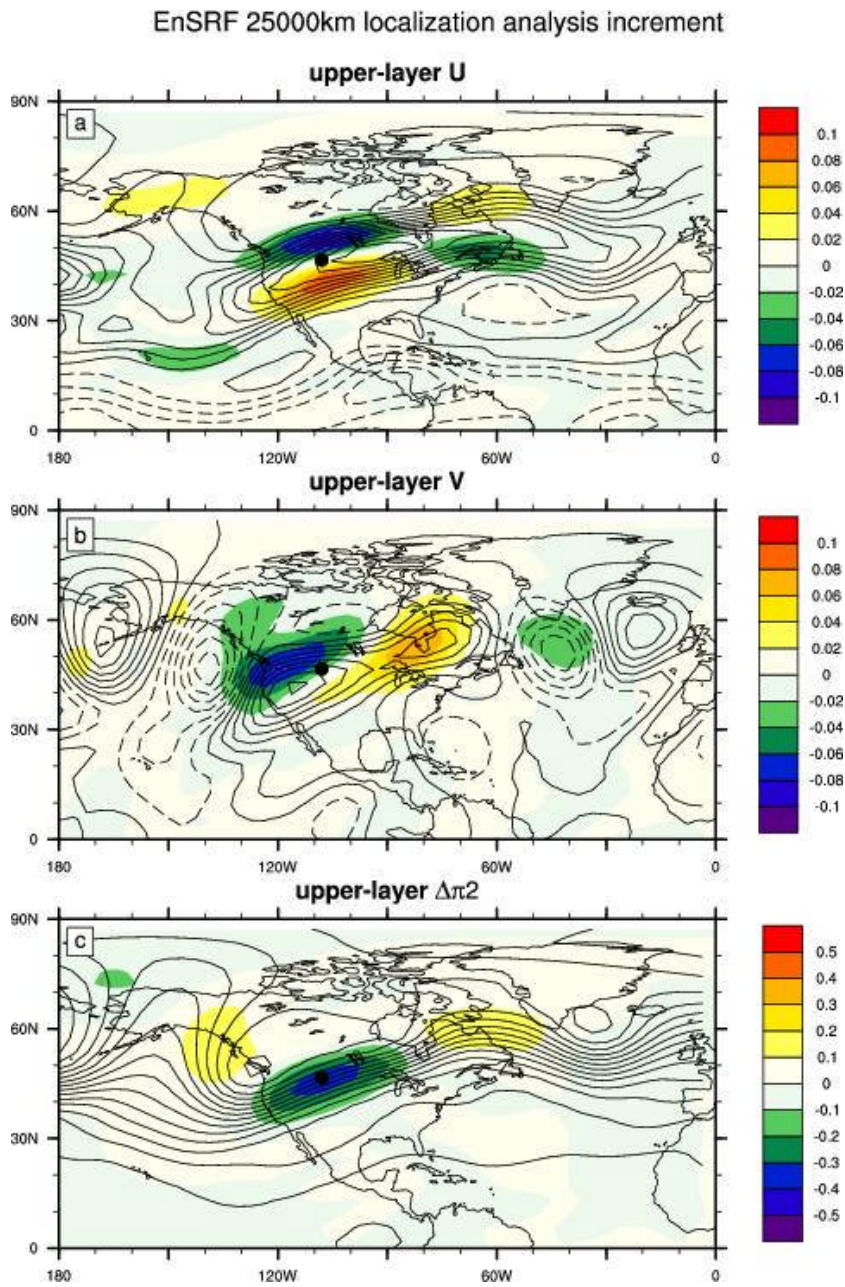


Fig. 5: Same as Fig. 4, except for the EnSRF with localization scale of 25000 km.

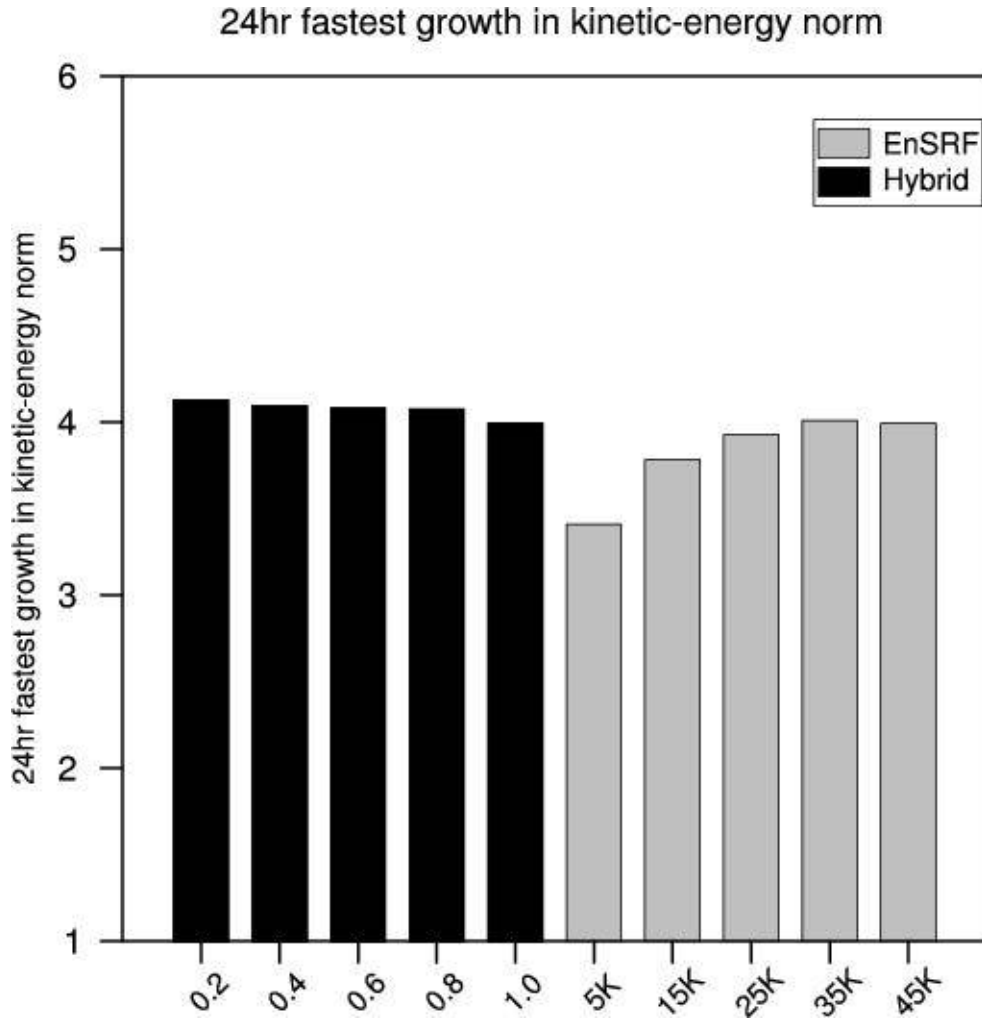


Fig. 6: Maximal 24-h perturbation growth in global kinetic-energy norm within the ensemble perturbation subspace for the hybrid ETKF-3DVAR (black bars), with different linear combination coefficients $\alpha = 0.2, 0.4, 0.6, 0.8$, and 1.0 , and the EnSRF (grey bars) with different covariance localization scales (5000km, 15000km, 25000km, 35000km, and 45000km).

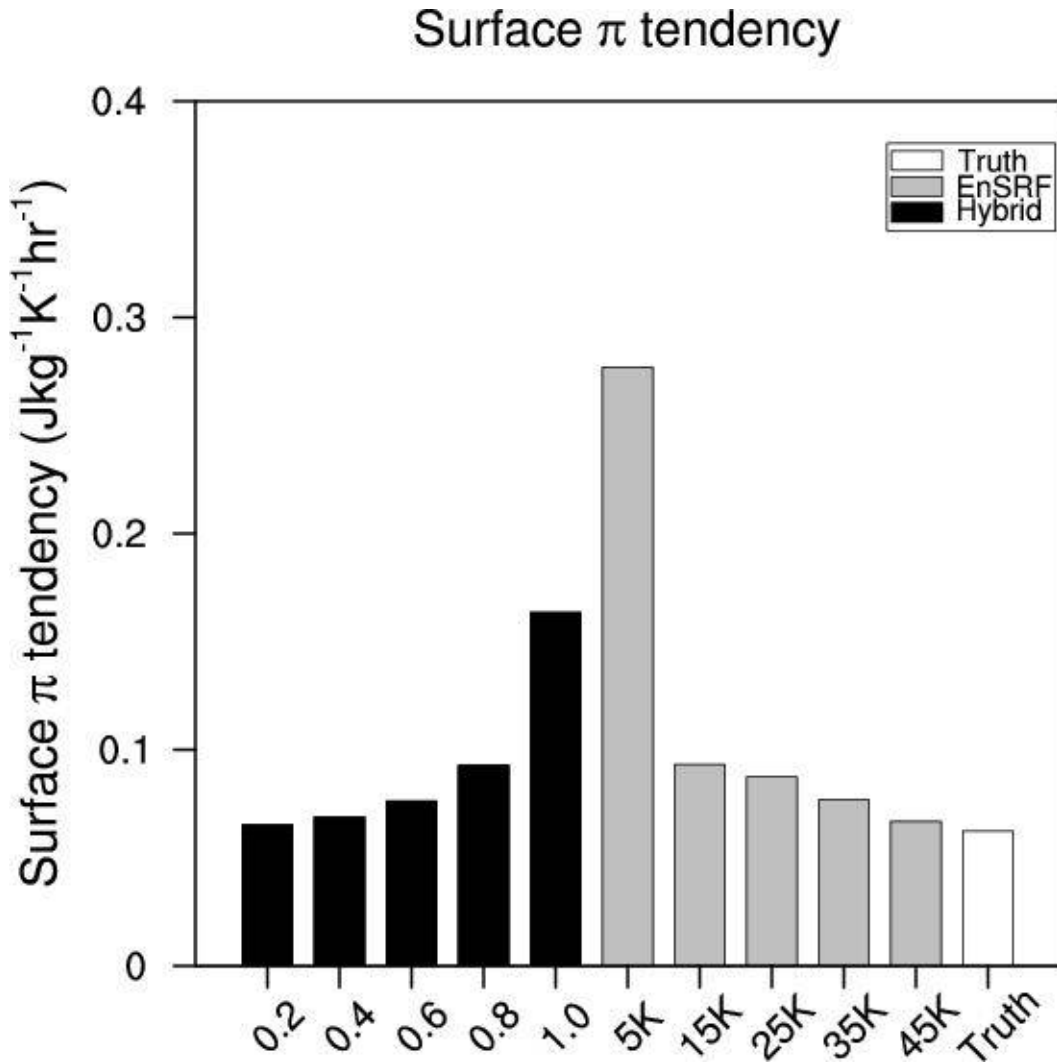


Fig. 7: Mean absolute surface π tendency ($\text{J kg}^{-1} \text{K}^{-1} \text{h}^{-1}$) averaged globally, over the subsequent 23 1-h forecast periods and over all ensemble members. The black bars are for the hybrid ETKF-3DVAR with different linear combination coefficients $\alpha = 0.2, 0.4, 0.6, 0.8$, and 1.0 , and the grey bars are for the EnSRF with different covariance localization scales (5000 km, 15000 km, 25000 km, 35000 km, and 45000 km). The white is for the truth.

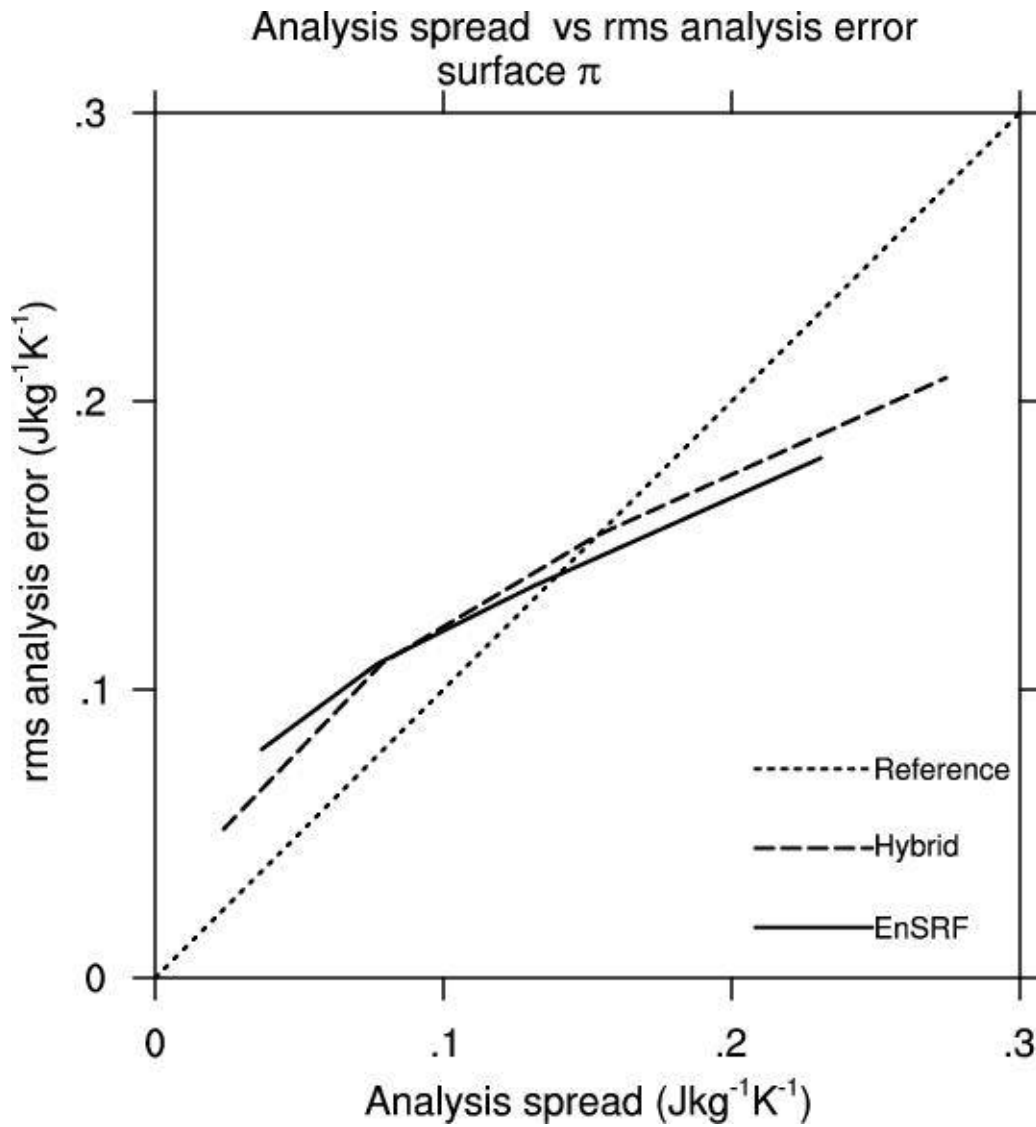


Fig. 8: The relationship between the surface π analysis spread and rms analysis error for the hybrid ETKF-3DVAR (dashed) and the EnSRF (solid). The dotted line is a reference line for a perfect ensemble.